Am J Physiol Lung Cell Mol Physiol 306: L897–L914, 2014.
First published March 21, 2014; doi:10.1152/ajplung.00007.2014.

CALL FOR PAPERS | *Real-time Visualization of Lung Function: from Micro to Macro*

Preclinical anatomical, molecular, and functional imaging of the lung with multiple modalities

Seth T. Gammon,[1] Nathan Foje,[2] Elizabeth M. Brewer,[3] Elizabeth Owers,[2] Charles A. Downs,[4] Matthew D. Budde,[5] W. Matthew Leevy,[2] and My N. Helms[3]

[1]*Department of Cancer Systems Imaging, The University of Texas MD Anderson Cancer Center, Houston, Texas;* [2]*Department of Biological Sciences, Notre Dame Integrated Imaging Facility, Notre Dame, Indiana;* [3]*Department of Pediatrics Center for Cystic Fibrosis and Airways Disease Research, Emory University, Atlanta, Georgia;* [4]*Nell Hodgson Woodruff School of Nursing, Emory University, Atlanta, Georgia; and* [5]*Department of Neurosurgery, Medical College of Wisconsin, Milwaukee, Wisconsin*

Submitted 7 January 2014; accepted in final form 20 March 2014

Gammon ST, Foje N, Brewer EM, Owers E, Downs CA, Budde MD, Leevy WM, Helms MN. Preclinical anatomical, molecular, and functional imaging of the lung with multiple modalities. *Am J Physiol Lung Cell Mol Physiol* 306: L897–L914, 2014. First published March 21, 2014; doi:10.1152/ajplung.00007.2014.—In vivo imaging is an important tool for preclinical studies of lung function and disease. The widespread availability of multimodal animal imaging systems and the rapid rate of diagnostic contrast agent development have empowered researchers to noninvasively study lung function and pulmonary disorders. Investigators can identify, track, and quantify biological processes over time. In this review, we highlight the fundamental principles of bioluminescence, fluorescence, planar X-ray, X-ray computed tomography, magnetic resonance imaging, and nuclear imaging modalities (such as positron emission tomography and single photon emission computed tomography) that have been successfully employed for the study of lung function and pulmonary disorders in a preclinical setting. The major principles, benefits, and applications of each imaging modality and technology are reviewed. Limitations and the future prospective of multimodal imaging in pulmonary physiology are also discussed. In vivo imaging bridges molecular biological studies, drug design and discovery, and the imaging field with modern medical practice, and, as such, will continue to be a mainstay in biomedical research.

noninvasive lung imaging; image molecular events in vivo; PET/SPECT/CT; epithelial sodium channels (ENaC) and fluid clearance; PAO-P1-*lux* bioluminescence

THE ABILITY TO NONINVASIVELY image biomarkers, genetically encoded reporters, tracer compounds, and anatomical structure in animal models is becoming critical to studying the molecular and structural basis of pulmonary disease. In preclinical imaging, there are various types of instruments and associated probes used to acquire functional, molecular, and/or anatomical images of the body. These include bioluminescence, fluorescence, magnetic resonance imaging (MRI), planar X-ray, X-ray computed tomography (CT), and nuclear imaging with positron emission tomography (PET) or single photon emission computed tomography (SPECT). Here we provide an introduction to the technology behind each modality and review its application in the study of the functional, anatomical, and molecular changes in the lung that can lead to serious pulmonary disorders.

Address for reprint requests and other correspondence: M. N. Helms, Dept. of Pediatrics, Center for Cystic Fibrosis and Airways Disease Research, 2015 Uppergate Dr., Suite 314, Atlanta, GA 30322 (e-mail: mhelms@emory.edu).

Bioluminescence Imaging

In vivo optical imaging of bioluminescence relies on enzymatic generation of visible light that is emitted, typically, from reporter genes. The light signal is detected and captured with a charge-coupled device camera (CCD), which converts photons striking each pixel into electrons to generate images with organ and suborgan spatial resolution. Since mammalian cells, unlike plant cells, have little or no innate bioluminescence and only limited autoluminescence (121, 138), the acquired images are often easy to interpret by using this modality. Linear relationships can be easily quantified with high signal-to-noise ratios and large linear dynamic ranges can be obtained over four orders of magnitude.

Bioluminescence imaging (BLI) can be further enhanced by using supercooled CCD systems with dark interior imaging

chambers that prevent stray light from entering the imaging field. These enable the sensitive detection of very faint luminescent signals at levels undetectable by the human eye. Well-designed digital imaging systems often incorporate cameras with well-controlled, uniform noise at high binning states and couple them to high-speed lenses. Because of the sensitivity of these systems, investigators must utilize materials, particularly plastics, paints, surgical tape, and fabrics that have low levels of phosphorescence, which can be mistakenly registered as "bioluminescence" and therefore generate imaging artifacts. Finally, when evaluating or building imaging systems there are other design factors to consider and balance, such as blooming (light spill from one pixel over to another), linearity (the linearity of the gray level response to photon input), hot pixels (bright spots that can be corrected by filling in with median value of surrounding pixels), image corruption (saturation of pixels due to cosmic rays and camera effects), and possible residual images (remaining charge from previous image leaving "ghosts"), to name a few. These BLI artifacts are often overcome with software correction.

Once images are acquired, BLI signal is often quantified in counts (38). Raw counts can be further normalized to the acquisition time (counts/s), area (counts·s·mm^{-2} or counts·s·cm^{-2}), or solid angle (counts·s·cm^{-2}·sr^{-1}) by calibrating the system to a known light source. Furthermore, by assuming a wavelength for an emitted photon (usually green), counts can be converted into photon-yielding units (photons·s·cm^{-2}·sr^{-1}). Alternatively, the light output can be converted from counts/s to pW, which does not assume a color of the photon being imaged. Each CCD has a different quantum efficiency curve; therefore, the units are relative to the particular imaging device utilized. As such, normalizing to counts/s and counts·s·cm^{-2} or counts·s^{-1}·mm^{-2} enables researchers to compare data from images acquired (from the same instrument) by using different acquisition times and binning states, which is often required in a longitudinal study in which emitted photon fluxes can change by orders of magnitudes.

There are also a few additional experimental considerations that should be addressed prior to conducting BLI in vivo (65). First, stable integration or transgene expression of the (luciferase) reporter construct should be verified, alongside optimizing the ideal concentration, timing, and point of substrate delivery. Light absorption and scatter are influenced by the target site and animal positioning; the signal decreases as the angle between the light source and optical plane increases, and postsurgical wounds can increase scatter (153). Because the BLI image is 2D and the resolution is 2–3 mm, BLI may not be able to differentiate between two distinct but adjacent signals. A device that is able to acquire 3D diffuse luminescent images (DLIT) is being developed to circumvent this problem (137). The impact of coat color on signal attenuation must be assessed, and whether depilation is required for optimal imaging of the thoracic area must be experimentally determined, as previously reported (162). Problems associated with light absorption by pigmented molecules and light scattering by fur can be easily overcome by depilation or shaving. Of course, another option is to use Harlan athymic nude mice (strain Nu/Nu), or nude hairless mice (strain SKH1) that lack fur, or albino BL6 strains that minimize the absorption and scattering of light by hair in BLI. (These strains are also particularly useful in fluorescence imaging as well). The lungs, in particular, represent a challenging environment for optical imaging due to the structure of the airways and alveoli. The presence of many overlapping and highly curved air/liquid interfaces cause significant scattering of light while imaging the lung, compared with imaging homogenous tissue (1). Thus probes and biomarkers developed and validated in other areas of the body will often require reoptimization when tested in the lung, even at equivalent tissue depths.

Generally speaking, BLI is based on the sensitive detection of visible light produced when a reporter enzyme oxidizes its luciferin substrate. The oxidation transiently converts the luciferin to a higher energy state, and when it relaxes back to the ground state a photon is released. Firefly, *Renilla*, and bacterial luciferases are the most commonly employed reporters in BLI studies. Specifically, luciferase proteins catalyze the oxidation of reduced luciferin in the presence of ATP and Mg^{+} (typically applied as cosubstrates in BLI assays) and oxygen to generate a yellow-green light emission of 562 nm at sufficiently high quantum yields (9, 40, 63). Green and red variants of luciferases have allowed for multiplexing of BLI reporters (24, 136). Coelenterazine, which is oxidized by an apoaequorin by-product, is responsible for the blue light emission of this reporter system (37, 97). Table 1 provides overview of the basic requirements, benefits, and limitations of commonly used luciferases for BLI. Importantly, since oxygen is a requisite cofactor for each of the enzymes listed, BLI assays cannot be conducted under strictly anaerobic conditions and its sensitivity will be significantly decreased during physiological hypoxia (i.e., hypoxia lung studies). This effect occurs not only because of the lack of oxygen but also (and likely more importantly) the decrease in metabolism and protein synthesis by mammalian and many bacterial cells at hypoxic sites. When quantifying BLI data, it is critical to utilize the same injection route and imaging time postinjection. Because the signal is dependent on the perfusion of the D-luciferin to the tissue, imaging times that are significantly different postinjection will yield different intensities even for the same site; for this reason intraperitoneal injections are often performed. For a nearly constant delivery of D-luciferin, researchers can also utilize osmotic pumps to deliver the substrate at a low, albeit constant level (64). BLI measurements are usually normalized to a control animal (at the same or similar anatomical site). Normalizing to different sites and different depths will confound data interpretation because of differential absorption and scattering of the two sites.

The *lux* reporter (101), which has readily detectable bioluminescence, has been particularly useful in studying bacterial gene expression and growth in vivo and has therefore been cloned into *Streptococcus pneumoniae* (59), tubercle bacillus (131), and gram-negative bacterial strains (110) to noninvasively monitor these pathogens in vivo. Viral infection and hosts can be studied in similar fashion by using firefly or click beetle luciferase genes (39, 131). BLI has been widely adopted by the cancer community to track metastatic lesions in the lung (75, 117). BLI, in combination with nuclear imaging (discussed below in the *Nuclear Imaging of the Lung: PET and SPECT* section), has also been successfully employed to study pulmonary inflammation (94).

Representative examples of *lux*-mediated BLI from in vivo and ex vivo specimens are presented in Fig. 1. The *lux* operon was cloned into a Mini-Tn7 vector and stably integrated into

Table 1. *Commonly used luciferases for bioluminescent imaging*

Enzyme	Size, kDa	Substrate	Cofactor(s)	Advantages	Disadvantages	Peak Emission, nm
Bacterial luciferase	α subunit: 40 β subunit: 37	$FMNH_2$	O_2, Decanal	Lux operon in bacteria can synthesize all required substrates and cofactors	Blue light emission limits sensitivity at deeper tissue sites Lux operon does not work in most eukaryotic cells	450
Cypridina (Vargula)	62	Vargulin	O_2	Bright, orthoganal substrate to both D-luciferin and Ceolenterazine	Blue light emission limits sensitivity at deeper tissue sites	460
Firefly and click beetle luciferases	61	D-Luciferin	O_2, ATP, Mg^{2+}; (acetyl-CoA not required)	Long history of use, stabilized, red/green-shifted luciferase available enabling the imaging of multiple pathways simultaneously	Variability of emission color with salt, temperature, and pH; variability in emission intensity with acetyl-CoA concentration	Firefly: 560, 613 (low pH and high temperature) click beetle red: 613 click beetle green: 537
Gaussia	19.9	Coelenterazine	O_2	High in vitro sensitivity, secretion of Gaussia luciferase allows for subject-independent measurements in vitro or ex vivo	Background due to oxidation of coelenterazine by serum, coelenterazine is a substr ate for MDR1-pgp; blue light emission limits sensitivity at deep tissue sites	470
Metridia	24	Coelenterazine	O_2	High in vitro sensitivity	(See Gaussia)	470
Renilla	36	Coelenterazine	O_2	Stabilized and green-shifted variants available	(See Gaussia)	470

the *Pseudomonas aeruginosa* strain PAO1-P1 (44) and was a kind gift from Dr. Joanna B. Goldberg. The PAO-P1-*lux* cells were grown overnight in 50 ml Pseudomonas isolation broth (PIB), pelleted, resuspended in phosphate-buffered saline (PBS), and imaged in Fig. 1, *A* and *B* (ex vivo). Next, 50 μl of PAO-P1-*lux* cells reconstituted in PBS were tracheally instilled via direct injection into the exposed trachea and the lungs were excised en bloc (as methodically described in Refs. 62, 72) to show bioluminescence of the reporter gene in situ (ex vivo); Fig. 1, *C* and *D*. Next, in vivo BLI imaging of PAO-P1-*lux* are presented in Fig. 1, *E* and *F*. Approximately 5 μl/g body wt solution was tracheally injected while animals were under anesthesia. All procedures have been previously reviewed and approved by Emory University Institutional Animal Care and Use Committees (62). It is important to note that the images shown were acquired immediately (within minutes) of PAO-P1-*lux* cell instillation; hence the study represents successful detection of targeted bacterial delivery and is not indicative of *P. aeruginosa* lung infection, which is beyond the scope of this review. The gray arrow indicates the site of tracheal instillation. The signal above the gray arrow comes from nasal escape of instillate compound and is expected in respiring animals to some degree following tracheal instillation. Importantly, the green arrows point to delivery of PAO-P1-*lux* into the distal portions of the lung (i.e., alveoli). All bioluminescent images (ex vivo and in vivo) were obtained by using 2 × 2 binning and a 15-min exposure time. Intensity bars are provided (photons·s^{-1}·mm^{-2}) to compare relative intensities between in vivo and ex vivo detection of bioluminescence. The robust and stable signal intensities of PAO-P1-*lux* detection in the lung allow for several exciting future research possibilities utilizing *lux* reporters and BLI related to pathogen invasion.

Since BLI is relatively straightforward to perform and results are easy to quantify and interpret, it has numerous important applications in preclinical research. For example, developing an appropriate method for delivering therapeutic genes effectively into the lungs to treat cystic fibrosis is an area of active research requiring BLI. In particular, researchers are utilizing luciferase gene expression to optimize the efficiency of viral and nanoparticle delivery and stable integration of genes in the lung. Since BLI is noninvasive, researchers can easily utilize this modality to optimize the dose and timing of gene delivery in a single powerful experiment (19, 26, 82, 157).

BLI of luciferin has also been reliably utilized as a method for measuring gene promoter activity in murine models of human respiratory disorders (103). In one specific example, transgenic mice were engineered such that luciferase was linked to the NF-κB inflammation pathway. Two cohorts of these mice were injected with adoptively transferred macrophages to assess the role of MAP kinase phosphatase 5 (MKP-5) in protecting against sepsis-induced acute lung injury (ALI). The adoptively transferred macrophages were obtained from either wild-type or MKP5-deficient mice and injected into mice that were subsequently dosed with LPS to initiate lung inflammation. Bioluminescence from the thoracic cavity of mice showed significantly higher signal intensity in mice receiving MKP5-deficient macrophages and was validated

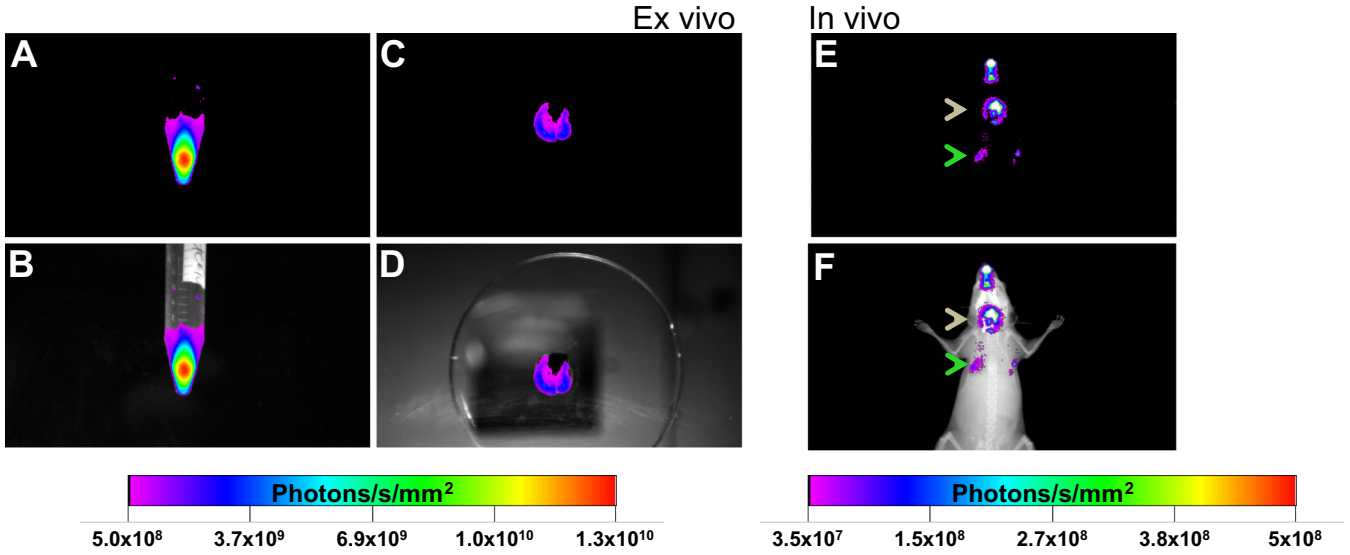

Fig. 1. Bioluminescent imaging. *A* and *B*: *Pseudomonas aeruginosa* strain, PAO1-P1, expressing the *lux* bioluminescent reporter gene (PAO-P1-*lux*) were grown in well-aerated shake flasks at 37°C in 50 ml Pseudomonas isolation broth (PIB) medium to an OD_{600} between 1 and 2 units. Four milliliters of the cultured PAO1-P1-*lux* cells were pelleted, resuspended in phosphate-buffered saline (PBS), and imaged for bioluminescence. In *B*, bioluminescence imaging (BLI) was overlayed with white light image of the test tube. *C* and *D*: PAO1-P1-*lux* resuspended in PBS (100 μl) was tracheally instilled into C57Bl/6 lung and excised for luminescence imaging. In *D*, the BLI was overlayed with white light image of petri dish. *E* and *F*: in vivo imaging of 100 μl tracheally instilled PAO1-P1-*lux* (resuspended in PBS). Gray arrow indicates site of tracheal injection of bacteria. Green arrow indicates PAO1-P1-*lux* luminescence in freely breathing anesthetized C57Bl/6 mouse lung. BLI was overlayed with image of mouse for anatomical coregistration in *F*.

against ex vivo data showing that MKP5-deficient macrophages produce greater amounts of cytokines following LPS treatment (119). Using a similar bioluminescent imaging approach, Mora et al. (104) characterized IκBα-(ΔN)-MTS as an effective inhibitor of the NF-κB signaling pathway in vivo. The general architecture of a promoter driving a luciferase or a luciferase fused to a protein is a broadly applicable strategy that has been used for a variety of pathways and is readily extensible to new research initiatives (87).

Fluorescence Imaging

Fundamentally speaking, fluorescence imaging differs from BLI in that the signal is generated by exciting a molecule with filtered light, as opposed to a chemical reaction, and a longer wavelength of light is emitted from the excited state. A filter is placed in front of the camera to block the reflected excitation light but allow the longer wavelength (emitted signal) to pass through. Unlike BLI, however, autofluorescence of tissue (especially in the blue/green wavelengths) commonly occurs. Nonetheless, in vivo imaging of fluorescence empowers researchers to observe biomolecules in both living and fixed cells at macroscopic and microscopic levels, respectively.

Photon attenuation and scatter (potentially generating autofluorescence) are the two major limitations associated with whole animal imaging in general (and is not limited to only lung imaging). For in vivo studies, it is preferable to utilize fluorophores with longer emission wavelengths near the infrared range (690–1,000 nm) over those that emit in the shorter, green area of the spectrum [for example, green fluorescent protein (GFP)]. The rationale for this is manifold: *1*) the infrared-shifted spectra typically provides higher signal-to-background noise, *2*) there is lower absorbance of near-infrared wavelengths in tissue, and *3*) less light is scattered in the longer infrared range compared with the shorter wavelength range of the spectrum. Although near-infrared reporters are becoming increasingly common for in vivo animal studies (discussed below), there are indeed strategies that have been employed to circumvent photon attenuation and autofluorescence that may be applicable to enhancing lung imaging studies, especially if conventional GFP probes are employed with very low signal accumulation at the target site. Under this less-than-ideal experimental scenario, spectral unmixing algorithms may be useful in separating the fluorescence background signals and accentuating the target emission (60, 61). Multiple fluorescent signals that differ by as little as 5 nm in peak position have reportedly been separated during in vitro quantum dot studies (61). Extending this spectral unmixing strategy in vivo will be challenging because these highly multiplexed systems use a single blue or UV excitation light, which will be strongly attenuated by tissue. Since the decay lifetimes of endogenous fluorophores are ~1–7 ns (21), late time gating (i.e., capturing the signal at a delayed time following excitation of the fluorophores of interest) can be used as an alternative strategic approach for detecting signal intensities above tissue autofluorescence (43, 66). An overview of the endogenous fluorophores (involved in metabolic processes and cell structure for example) is discussed in Ref. 22.

There are numerous fluorescent proteins, dyes, and probes that enable the study of gene expression, protein structure/localization, cell signaling, growth, and apoptosis. Figure 2*A* illustrates the spectral profiles of fluorescent proteins that are commonly conjugated to antibodies, vital dyes, or molecular probes to directly (i.e., activated probes) or indirectly (i.e., reporter gene) assay for biomolecular processes of interest. Challenges in imaging the lung by use of fluorescent probes include the effective delivery or targeting of the compound into the lungs (i.e., via minimally invasive nasal aspiration or direct tracheal instillation into the lungs) and the requirement that the

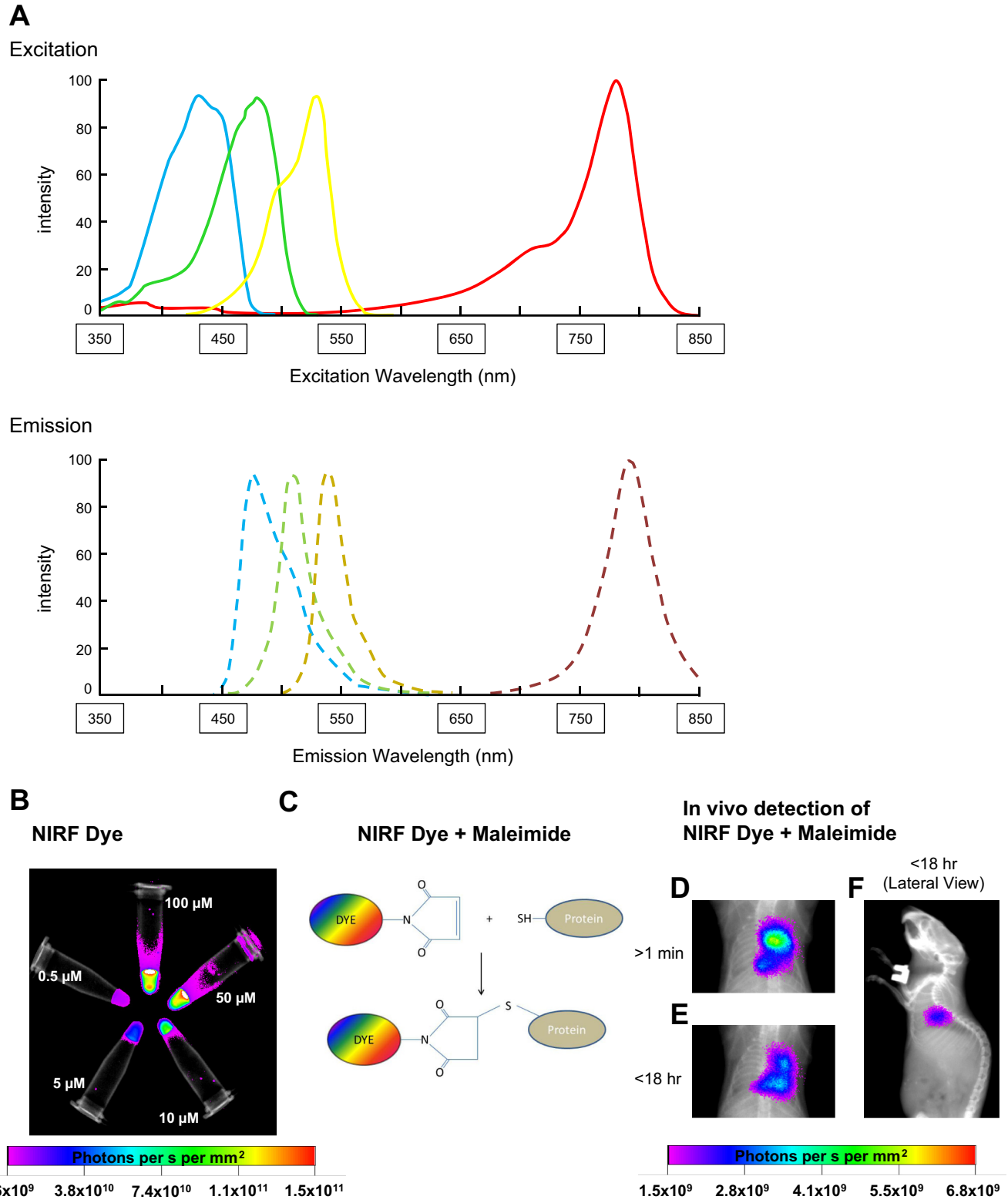

Fig. 2. Fluorescence molecular imaging. *A*: excitation and emission wavelength spectra of fluorophore conjugates commonly used in macro and micro imaging. *B*: fluorescence emission of 0.5–100 µM (50 µl) near-infrared dye (NIRF). *C*: schematic depicting NIRF conjugation to maleimide compound and labeling reaction with sulfhydryl (-SH) groups on protein. *D*: in vivo detection of NIRF-maleimide labeling of -SH groups immediately following tracheal instillation of 400 µM dye (>1 min) into C57Bl/6 mouse lung. *E*: posterior view of NIRF-maleimide labeled lung (shown in *D*) ~18 h posttracheal instillation. *F*: lateral view of C57Bl/6 mouse described in *D* and *E*. In *D–F*, signal intensities have been contrasted to emphasize retention of NIRF-compound in the lung.

probe must stay biologically active and is not immediately cleared by the mucociliary escalator (able to filter out particles between 2 and 10 μm). These issues are not unique to fluorescence imaging but apply to any imaging modality that requires administration of a contrast probe or tracer. To circumvent these challenges related to effective delivery and retaining the probe/tracer compounds in the lung (air space), our laboratory routinely delivers reporter compounds via direct tracheal instillation using dosages that are several folds higher than the effective concentration applied in vitro.

Like bioluminescence studies, the units in a fluorescence image are counts, fluorescence units (FU), arbitrary units (AU), or relative light units (RLU). These units can then be normalized to acquisition time in counts/s, and to excitation power or fluorescence "efficiency." In vivo fluorescence measurements are typically made in a ratiometric fashion, in which the signal is divided by that from a control animal, to the same anatomical location on a specimen at an initial time point, or to a contralateral, "nontarget" site on the same animal. These ratios may be tracked over time to yield a semiquantitative output for longitudinal measurement. This is very important in fluorescence, since the power of excitation lamps varies between acquisitions, even if performed on the same day. To control for this innate variability in the energy source, the most ideal experimental setup for a fluorescence imaging assay would be to include a positive fluorophore emission signal control within the optical field of each acquisition that may be utilized for calibration and/or normalization of the experimental outcome. Practically, however, small animal imaging systems can often house multiple animals, and therefore baseline measures of fluorescence are typically acquired by using an (in vivo) control animal for normalization of experimental outcome. Because fluorescence uses a wide range of wavelengths, these units are rarely converted into photons and are presented as AU events normalized via ratiometric analysis.

The use of microscopic and macroscopic fluorescence imaging has indeed expanded into almost every discipline of biomedical research and discovery (which goes beyond the scope of this review). A comprehensive review of near-infrared fluorescent (NIRF) probes that have been recently developed for preclinical imaging in small laboratory animals is presented in Ref. 123. Herein, we discuss a few contemporary applications of in vivo fluorescence imaging in the near-infrared range and show one example of optical imaging of biochemical events captured in vivo.

Figure 2*B* shows one example of a noninvasive application of a NIRF probe suitable for in vivo visualization and interrogation of pulmonary molecular signaling. In this particular study, NIRF-conjugated maleimide was purchased from LI-COR Biosciences (Lincoln, NE) and reconstituted in PBS, pH 7.4. Generally speaking, maleimide compounds are reactive toward free-SH (thiol, sulfhydryl) groups. As such, most proteins with reduced Cys amino acids can be labeled with NIRF-conjugated maleimide (see Fig. 2*C* for biochemical reaction). In Fig. 2*D*, NIRF-maleimide (400 μM) was reconstituted in PBS and tracheally instilled (50 μl) into depilated C57BL/6 mice. Animals were placed into an in vivo image station (760 nm excitation; 830 nm emission, 30-s exposure time, and 55.2-mm field of view) immediately following instillation (>1 min postoperative). Since the tracheal instillation and imaging procedures are minimally invasive, the same animals were viable and reimaged ~18 h posttracheal instillation with the NIRF-maleimide compound (Fig. 2, *E* and *F*, posterior and lateral views, respectively). This longitudinal study indicates that the bound NIRF dye is indeed stable in the lungs of living mice. Importantly, the light output from control or baseline studies can be quantified and compared against experimental groups. This is one of many examples of how near-infrared imaging enables investigators to obtain biochemical information (with high signal to low noise) related to the molecular landscape and redox environment of the lung. These translational imaging studies would indeed complement standard molecular biological assays and/or in situ lung studies evaluating Cys thiol modifications.

Kundu et al. (88) generated a family of hydrocyanine sensors (hydro-Cy3, hydro-Cy5, hydro-Cy7, hydro-IR-783, and hydro-ICG), which increased in fluorescence intensity 100-fold following oxidation by either superoxide or the hydroxyl radical. These compounds are highly suitable for in vivo imaging of oxidative stress. Specifically, these compounds have nanomolar sensitivity toward the hydroxyl radical and are therefore more sensitive than dihydroethidium, which is also commonly used to measure intracellular reactive species (49). However, the hydrocompounds that fluoresce at high emission wavelengths (660–830 nm) are more suitable for imaging reactive oxygen species (ROS) production in vivo (88). We have recently imaged ROS production in the lungs of C57BL/6 mice following an LPS-mediated inflammatory response compared with mice receiving LPS in combination with a small G protein inhibitor, which blocks NADPH oxidase production of ROS (62). In this study, it was shown that the fluorescence intensity of hydro-Cy can be used as an indicator of the oxidative state of the lungs imaged in vivo. Using the same redox sensitive compound, Kundu et al. verified that changes in fluorescence intensity (i.e., oxidative stress) were similar whether the fluorescence signal was imaged in vivo or whether tissue explants were analyzed by confocal microscopy following LPS exposure. This highlights one excellent benefit of fluorescence: the ability to use macro- and then microimaging systems to confirm experimental outcome.

Given the exquisite use of quantum dots in the detection of vascular endothelial cell adhesion molecules (VCAM) during lung inflammation performed by the Chatterjee group (109), we anticipate continued expansion and refinement of preclinical imaging assays incorporating the use of quantum dots in the near future.

Planar X-ray Imaging

Medical X-ray imaging utilizes photons with much shorter wavelengths than visible and ultraviolet light, ranging from 10^{-3} to 10^{0} nm (shown in Fig. 3*A*). Within this range, X-rays are widely used in medical imaging because of their ability to penetrate tissue. A radiograph is produced when X-rays pass through hard and soft tissue, with variable efficiency directly related to tissue density, onto a photographic plate or digital recorder. The output image is typically grayscale and may be thought of as a shadow of the object in the path of the X-ray beam. In a classic X-ray image with film, areas that appear white represent dense tissues (like bone or inflammation and infected lung tissue that can obstruct the passage of X-ray energy). Meanwhile, tissue that is not dense (like the lungs,

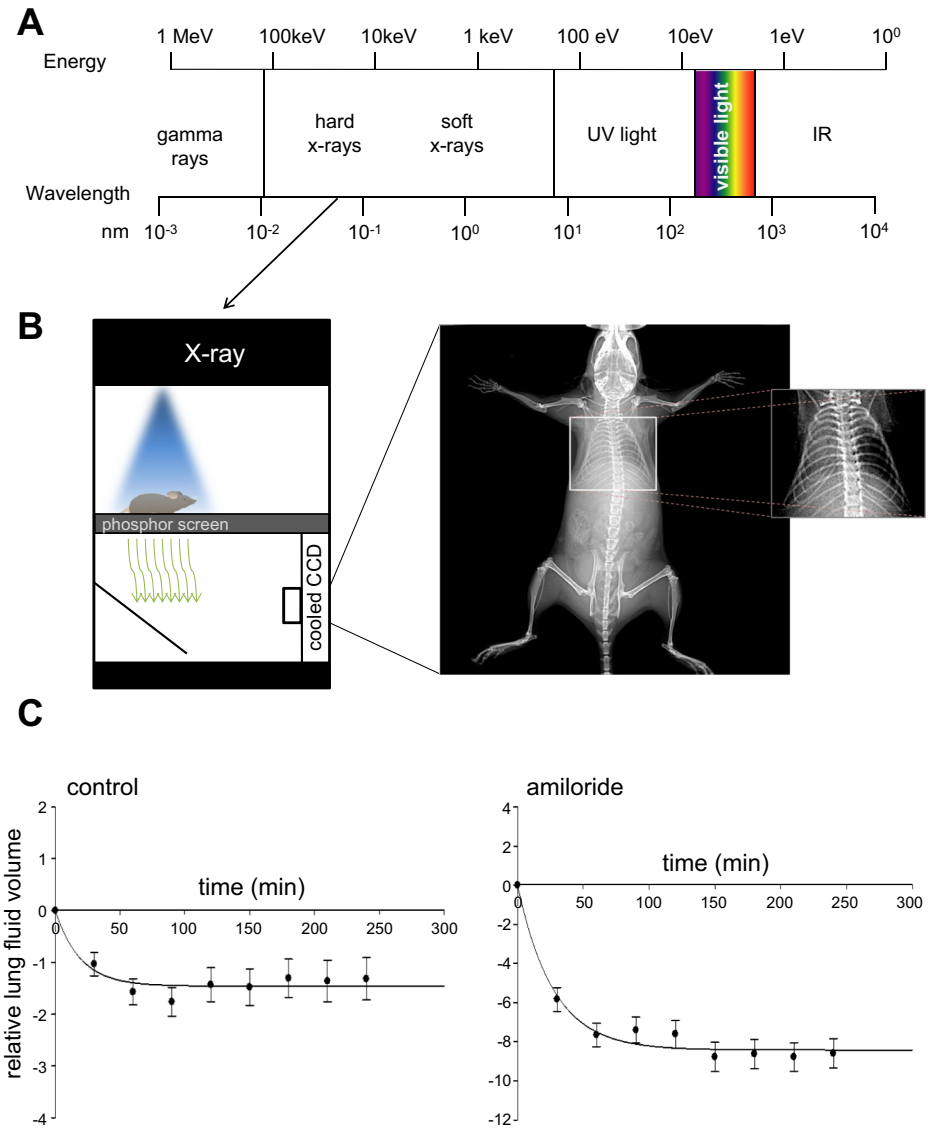

Fig. 3. Imaging. *A*: photon energy and wavelength of hard and soft X-rays in relation to gamma rays, ultraviolet (UV) light, and the visible spectrum (IR = infrared). *B*: typical image device layout for imaging. CCD, charge-coupled device camera. *C*: representative whole body. Thoracic region highlighted and software enhanced to emphasize alveolar flooding (following tracheal instillation of saline) in the anterior aspect of the left lobe of the lung. The air-filled lobes of the right lung do not attenuate photons and therefore appear black in images. *C*: quantification and normalization of control (saline-treated; K = −1.458; Ka = 0.052) and amiloride treated lungs (K = −8.427; Ka = 0.037) shows that imaging can be used to measure real-time changes in lung fluid volume and reveal molecular changes in net salt and water reabsorption in alveoli (see text for details).

which are filled with air) will have contrast at the opposite end of the grayscale spectrum and appear black. For pulmonary imaging, the bones of the rib cage and vertebral bodies will appear white, the lungs will appear black, and the heart will be a shade of gray. Dense lung tissue, as occurs with severe pulmonary fibrosis, atelectasis, and pulmonary edema (to name a few examples), appear gray to white on a chest X-ray with a black palette of normal lung tissue. With modern digital X-ray technology, these color scales can be optimized to achieve the best contrast for a given feature/disorder.

With conventional X-ray imaging, the rate of lung fluid clearance in freely breathing-anesthetized mice has been assessed in a model of aspiration pneumonia (62, 143). In our studies, animals were X-ray imaged with acquisition periods of 120 s and X-ray density was quantified as an expression of lung fluid volume and normalized to the initial X-ray intensity (Io) as a function of change in lung fluid volume at any given time (I), where I-Io represents the difference in X-ray opacities (for example, before and after fluid clearance). This holds true so long as the material studied is in the linear range of the assay. For broader ranges of mass, it is useful to convert the imaging data into X-ray density units (which are analogous to absorbance units in UV/Vis Spectroscopy). After "flattening the field" to normalize for variation in X-ray exposure delivered by a cone beam, the intensity in a given pixel is $-\log(I/I_{mean})$ where I_{mean} is the average brightness for that exposure time when no sample is present. The amount of X-ray attenuating material above this pixel is now linearly proportional to X-ray density over a broad range of absorbance values. Below, we provide one example as to how pulmonary function (alveolar fluid clearance) and molecular mechanisms (regulating ion transport) can be gleaned from X-ray imaging.

Figure 3*B* shows a representative planar X-ray image of tracheally instilled lung, in which the anterior aspect of the left lobe has been flooded with saline (methodically described in Ref. 62 and reviewed in Ref. 50). Software analysis of the X-ray opacities allowed for detecting very small (μl) volume changes in lung fluid volume over a 240-min time frame. Furthermore, fitting these data to the model $F(t) = K(1 - e^{-k}a^{t})$, where $F(t)$ represents the amount of surface fluid in the

lung at time, t; K is the steady state or peak amount of lung fluid; and k_a is the rate of fluid absorption, the rates of secretion can be determined by dividing the peak fluid volume by the rate of absorption (K/k_a) (143). This expression allows for comparison of the rate of lung fluid clearance among experimental groups. In Fig. 3*C*, the attenuation differences of saline- and amiloride-treated lungs were plotted and fit to the aforementioned equation to serve as one example of how X-ray imaging can be refined to provide useful information on the rate of lung fluid clearance, and secretion, in C57Bl/6 mice following treatment. As expected, amiloride inhibited the open probability of epithelial sodium channels (ENaC) responsible for net salt and water reabsorption in the lung. As a result, the rate of clearance in C57Bl/6 mouse lung is significantly attenuated, as reflected by smaller calculated I-Io values (i.e., gray X-ray opacities). The interested reader is referred to the following papers that utilized X-ray imaging to delineate the signal transduction pathway regulating lung ENaC and fluid volumes (51, 52, 62, 84, 143).

Phase-contrast X-ray imaging represents a new technological variation in which the object and detector are separated by a short distance to allow refracted X-rays to diverge from the undeviated photons. Using phase-contrast X-ray methods, several studies have generated clear images of aerated lungs in small laboratory animal models (83–85). Lewis et al. (95) utilized this technology to image the lungs of rabbit immediately after birth. In these studies, all objects were positioned ~210 m downstream of the synchrotron (particle accelerator) source, with a detector placed 3 m downstream to record the phase-contrast images. In these particular studies, newborn rabbit pups were imaged at 4-s intervals for the first hour after birth with 588-ms exposure times. Volumetric changes in lung fluid in this dynamic study were evaluated by implementing an algorithm previously described in Ref. 85.

X-Ray Computed Tomography

CT is an anatomical imaging modality with widespread clinical and preclinical utilization. CT functions by taking planar X-ray images at defined angles around the subject by means of a gantry-based system. These X-rays are then compiled and reconstructed via a filtered backprojection algorithm (111) to produce a 3D array of voxels that encode radiodensity values in Hounsfield units (HU). The HU scale extends from values of −1,000 for air, to 0 for water, and 1,000–3,000 for bone of varying density. Although CT is often used to visualize structures with high X-ray attenuation, it is also useful for imaging lung tissue because its unique low density of approximately −500 HU, owing to the presence of air. Thus CT enables the quantitative measurement of the volume and density of lung tissue and permits the visualization of regional changes in anatomical structure.

Two key aspects of a given X-ray CT device are its resolution and associated radiation dose. Although resolutions of ~1–5 mm are typically obtained in the clinic using regular CT, the smaller anatomy of mice demands finer detail. Thus in vivo microCT systems have been developed to achieve resolutions of ~0.1–1 mm with voxel sizes ranging between 10–500 μm. Note that voxel size and resolution are two distinct values, and it takes multiple voxels to resolve a structural feature within an image. For example, a data set with 1-mm resolution would use voxels with sizes of 250–500 μm. Voxel size alone does not define the image resolution, but this is often the primary parameter that is listed on a specification sheet or in a methods section. In this case, the features that can safely be delineated must be larger than the voxel size by at least two- to threefold. Overall, the image resolution will depend on many factors related to the caliber of the X-ray source and detector, as well as the quality and number of the raw data projections that are generated, and can be evaluated through the use of image phantoms (135). In general, systems operating in the 0.1–1 mm resolution window (microCT) do not impose a lethal radiation hazard on the specimen (80–160 mGy) safe range (144, 155), although studies have shown this level may alter the biology of the system under study (111, 126). Higher resolution in vivo microCT scanners are available that can delineate features in the 10- to 30-μm range. However, this is achieved via acquisition of additional projections (i.e., longer exposure), with the X-ray source closer to the specimen under study to achieve geometric magnification. This results in an increased dose that may exacerbate the radiation induced biological changes. For this reason, research groups are working to optimize scan parameters to maximize resolution while minimizing dose at all levels of resolution (135, 155).

The tomographic data from a CT scan is typically viewed in one of two ways. The first involves presenting the data as a slice through the sagittal (side), coronal (top), or transverse (axial) planes. Figure 4, *A–C* present example grayscale slices of (normal) mouse lungs taken with an in vivo microCT scanner at a medium level of resolution (~500 μm resolution with a 125-μm isotropic voxel). One can note the presence of the heart, as well as pulmonary vasculature, on the dark palette of the lung air volume. Note that other methods exist for high-resolution postmortem CT imaging of mouse pulmonary vasculature (41), as well as ex vivo imaging of the structure of pulmonary acini (151). A second procedure for visualization of CT data of the lung involves a technique called segmentation, with subsequent 3D rendering. Automatic segmentation of healthy or diseased lung volume provides a powerful tool for quantitative analysis and visualization of the airway. This strategy uses software to automatically segment areas within a given range of HU that are specific to lung. This segmentation will create an independent data set that can be coregistered with the mouse CT to give an output such as that presented in Fig. 4*D*. In this case, the segmentation values were set to −550 to −200 HU to capture the healthy lung air volume, and the ensuing data set was rendered in blue with the skeleton in grayscale. Severe lung injury and disorder make automatic segmentation a challenge. There are several methods employed, such as atlas-based segmentation (139), an adaptive border algorithm that includes nodules (118), adaptation of thresholds for individual patients based on curvature of the ribs (116), and a hybrid lung segmentation approach (149), to name a few. A thorough topical review on automated segmentation in normal and diseased lungs can be found in Ref. 150. A grand challenge on the segmentation of the lungs from CT scans was held in 2011 (LOLA11, www.lola11.com). Results from this grand challenge indicated that most segmentation methods performed efficiently in normal or emphysematous lungs, but that errors often occurred in lungs with severe abnormalities.

Previous studies have used microCT to study emphysema by quantifying the low-attenuation areas (LAA) in the lungs (48,

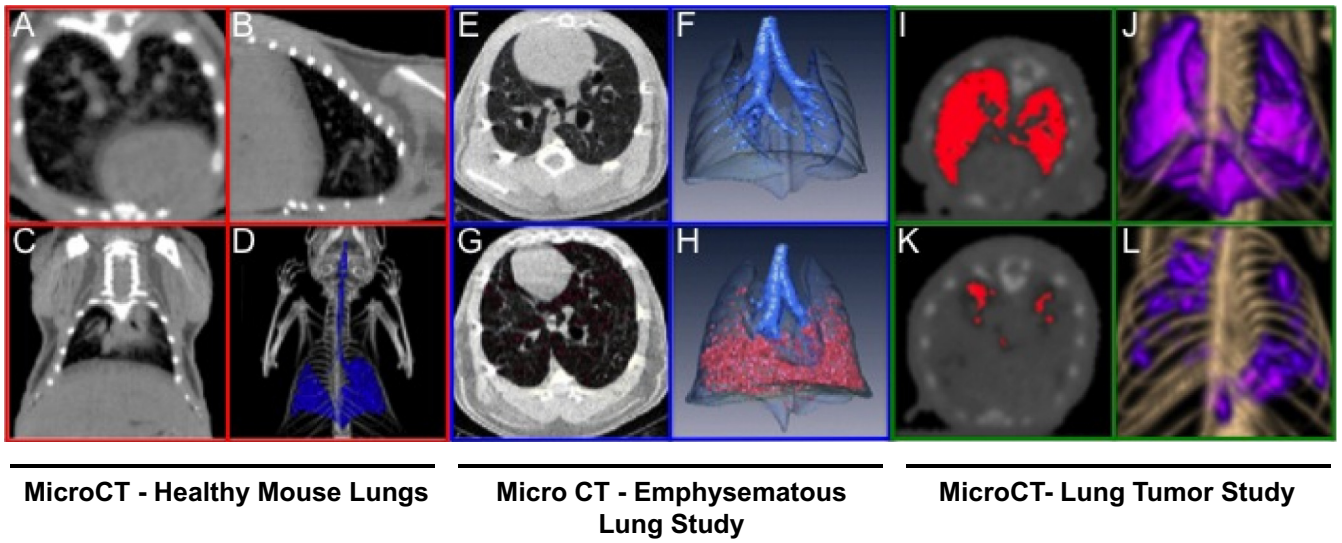

Fig. 4. MicroCT imaging of healthy, emphysematous, and cancer-damaged lung. Left section (red outline): transverse (*A*), sagittal (*B*), coronal (*C*), and false colored 3D rendering (*D*) of the lungs on a healthy mouse. Middle section (blue outline): transverse slices of a control mouse (*E*) and an emphysematous mouse at *week 2* (*G*). 3D renderings of control mouse (*F*) and emphysematous mouse (*H*) at *week 2* with normal structure in blue and emphysematous tissue in red. Right section (green outline): Transverse slices in tumor bearing mice at 2 wk (*I*) and 6 wk (*K*), with healthy lung volume segmented in red. 3D renderings of *I* and *K* respectively (*J* and *K*), with healthy lung in purple. *E–H* reprinted from Ref. 11 with permission. *I* and *K* reprinted from Ref. 46 with permission.

86), which represent destruction surrounding the air sacs. LAAs are marked by volumes with −960 HU. By tracking the LAAs over a specific amount of time, researchers were able to track the progression of emphysema. The center portion of Fig. 4 gives an example using LAAs to provide both quantitative and qualitative data from an emphysema disease model. Two groups of mice were used in this project: one control (Fig. 4, *E* and *F*) and one injected with elastase (Fig. 4, *G* and *H*), which caused severe emphysema over a period of ~2 wk. MicroCT scans were taken at high resolution (46 μm isotropic voxel with 716-mGy radiation dose) at various time points following injection, using a breath-hold gated technique in which the mice were artificially ventilated and the lungs inflated for 650-ms increments in which all projections were gathered. Regular CT scans of the lung, with no gating, capture the tissue in a noninflated state. The breath-hold gating technique increased the quality of the microCT images by using projections of the inflated lungs and improved the resolution of density values for the lung tissue (3, 12). The lungs were reconstructed and automatic segmentations gathered from the data (12, 144). Areas of healthy lung tissue in the normal density range were segmented and colored a light blue-gray color, whereas regions of lung tissue with values of −960 HU were independently segmented and colored red to highlight areas of emphysema.

Many groups have used microCT to study lung cancer (45, 105, 111). The right section of Fig. 4 shows an example of cancer growth in the lungs from a mouse model of metastatic breast cancer. As tumors grow within the lung, they encroach on the airways and diminish lung volumes (healthy air spaces appear black). The progression of tumor growth from *week 2* (Fig. 4, *I* and *J*) to *week 6* (Fig. 4, *K* and *L*) demonstrates progression of tumor growth depicted by the increase in gray contrast in the lung. Figure 4, *I* and *K*, gives transverse views of lung tissue with the healthy areas segmented and highlighted in red. Figure 4, *J* and *L*, shows 3D renderings of the data from Fig. 4, *I* and *K*, with healthy lung tissue highlighted in purple. These images were taken at a lower resolution setting with a 250-μm voxel size but were certainly adequate for longitudinal imaging and analysis of changes in lung volume and density (45). Given the noninvasive nature of microCT, these types of representative scans (shown in Fig. 4) may be repeated over several weeks, resulting in data that can be compared with determine the effect of various diseases on healthy lung volume.

In addition to emphysema and cancer, CT can also be used to study other serious respiratory disorders, such as asthma and fibrosis. Indeed, researchers have been able to quantify changes in the asthmatic lungs by using CT to determine the dimensions of narrowed airways (13, 76, 91, 92, 100). The stiffening of fibrotic lung tissue has also been evaluated via microCT (115). In one case, microCT was coupled with pulmonary gating to determine residual volumes (equivalent to the end-expiratory volume, EEV, in humans) of animal models with fibrosis (47). This volume can be tracked over a period of time to follow the progression of fibrosis.

There have been advances in digital radiography that have made it possible to utilize X-ray technology for kinetic studies related to lung tissue motion during breathing (i.e., 2D imaging of respiratory motion). Given the differences in X-ray attenuation coefficients at high and low X-ray energies, dual-energy chest radiography can enhance imaging of the lung by removing the bone signal from the images of soft tissue. The ability to remove artifacts in dynamic dual-energy imaging can, for example, aid in the prediction of lung tumor position during treatment with submillimeter precision and eliminate operator subjectivity in tracking tumor motion. Specifically, Xu et al. have utilized dual-energy chest radiography at 30 frames/s in preclinical studies to obtain regional lung information during ventilation of anesthetized swine (158). By analyzing lung density variation, these studies have demonstrated the feasibility of using X-ray based imaging in kinetic studies. Other advances have sought to refine the quality of CT images of the

lung. Note that, during the acquisition of a CT scan, the animal is freely breathing under anesthesia. About 70% of the projections will capture the lung in its noninflated state, whereas the remaining projections capture the specimen during inspiration (78). The reconstructed data are thus an average of the noninflated and breathing states but will be weighted to the noninflated condition since this will supply the majority of projections. Researchers have utilized various forms of gating to optimize the image quality of reconstructed CT data. During gating, the animal is attached to a sensor that detects respiration. In one case, the breathing data can be time synchronized with the capture of projections to eliminate those occurring during respiration (73). In other cases, a respiration event can trigger the imaging system to capture a projection of the lung in its inflated state, and the ensuing CT data will reflect this. This may also be done using "retrospective" gating, in which the projections capturing respiration are removed from CT reconstruction by computational methods (10). Retrospective gating increases the dose required for a similar contrast because projections are "thrown out" requiring longer acquisition times. Moreover, Dr. Farncombe (54) has proposed an additional method of CT respiratory gating that does not rely on external physiological monitoring; rather, the data are binned into inspiratory and expiratory phases, allowing for the calculation of various lung volumes. By using this alternative approach, respiratory tidal volumes can be estimated within 16% in rat and mouse animal models. In yet another scenario, the specimen may be ventilated, as noted above, and the lungs inflated for longer periods to capture high-quality projections of the inflated state to in turn yield quality tomographic data of this state (78). Continuous xenon-enhanced CT has enabled noninvasive monitoring of regional ventilation with temporal and spatial resolution in mechanically ventilated Wistar rats (89). Moreover, Badea and colleagues (14) have recently utilized the dual-energy CT imaging to show effective separation and reliable estimation of air, tissue, and blood volumes of the lungs in a preclinical setting.

In summary, the capture of microCT data in free-breathing animals will enable the noninvasive and high-throughput detection of a range of pulmonary diseases in mice, and advanced gating and dual-energy methods are available as needed to refine the spatial resolution and density measurements within the lung volume.

MRI and Noninvasive Monitoring of the Lungs

MRI is an imaging modality routinely used in the clinical setting and has excellent soft tissue contrast without harmful ionizing radiation. MRI is based on the intrinsic property of atomic nuclei to align with an external magnetic field and precess (i.e., resonate). Hydrogen nuclei (i.e., protons) associated with water molecules are the basis for most MRI applications. Radiofrequency pulses are used to perturb the nuclei from their equilibrium state, and applied magnetic fields (i.e., gradients) are used to encode spatial information to generate 2D or 3D images. The basis for contrast in MRI exploits the feature that nuclei within different tissues return to their equilibrium state (i.e., relax) at different rates. A wide variety of other physical phenomena such as flow and diffusion can be detected, and many of these specialized techniques have important applications to the study of lung development and disease. For example, pulmonary perfusion can be measured noninvasively by performing high temporal resolution imaging in conjunction with an intravascular bolus injection of a gadolinium-based contrast agent (102). The contrast agent alters the relaxation properties of nearby water molecules, and with appropriate pharmacokinetic modeling one can derive the relevant perfusion features such as transit time. In practice, respiratory motion must be minimized, and adaptations typically include rapid imaging methods or synchronization with respiration (71). Recent techniques such as ultrashort echo time acquisition has also improved the studies of ventilation and perfusion (18). Since the lungs have relatively low proton content, the utility of clinical MRI is often similar to that of CT, including visualization of the pulmonary vasculature and detection of abnormal pathological processes such as pneumonia or tumors situated in or near the lung.

The usefulness of MRI to image lung structure and function has been greatly expanded by the addition of hyperpolarized noble gases such as ^{3}He (57) and ^{129}Xe (57) as well as hyperpolarized metabolic substrates such as ^{13}C-pyruvate (146). Hyperpolarization is a process that alters the equilibrium state of the gases to allow their detection with MRI. The specialized equipment necessary for hyperpolarization is becoming more widely available and will facilitate the adoption to both preclinical and clinical settings. The hyperpolarized gases are inhaled immediately prior to collection of an image. Importantly, the gases are detected directly and enable visualization of the airways and air spaces in the lung (6, 29, 57, 79). These techniques can also be combined with other MRI methods and have opened a broad range of applications to image pulmonary structure and function in health and disease (122).

MRI has been extensively used for a range of preclinical lung disease studies. Zurek and Cremillieux (163) recently detailed a review on the application of MRI to pulmonary disorders. Here we provide a few recent examples to highlight the use of MRI for lung research in mice. Egger and colleagues (53) demonstrated the utility of MRI to detect pulmonary fibrosis in living mice and rats treated with bleomycin. Figure 5 displays a transverse slice of a rat lung before and 7 days after bleomycin treatment. Segmentation of high-intensity areas within the slice highlights the development of lung fibrosis and provides a means for quantitative assessment of the disease over time. Caravan and coworkers (25) improved the sensitivity to bleomycin-induced fibrosis in mice using a collagen-specific MRI probe that provided a twofold enhancement of the

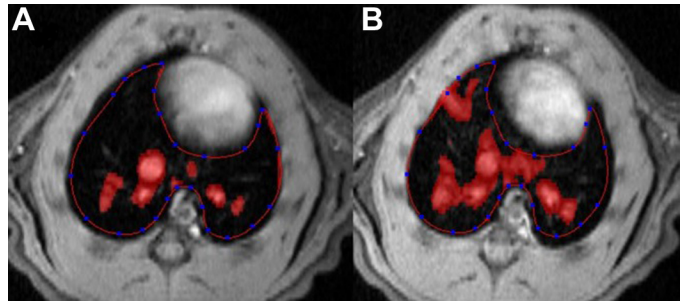

Fig. 5. Transverse MRI slices of rat lung before (*A*) and after (*B*) 7 days of bleomycin treatment to induce fibrosis. Red areas indicate high intensity regions detected through automatic segmentation. Figure reprinted from Ref. 53 under the terms of the Creative Commons Attribution License.

signal to noise ratio, a metric used to quantify image quality. MRI has also been utilized extensively to visualize pulmonary edema (17, 147). Whereas the lungs normally have low water content and appear dark on images, edema appears as conspicuous bright regions in a variety of animal models. In contrast, emphysema is detectable by traditional MRI as a loss of normal structure, as demonstrated by Takahashi and coworkers in mouse lungs (142). The effects of emphysema are more clearly visualized by hyperpolarized ^{3}He MRI in which the breakdown of lung tissue is readily evident (33, 112, 129). Finally, the detection of tumors within the lung space leverages the well-known strength of MRI for cancer imaging. Numerous MRI protocols exist to detect lung tumors in preclinical models of primary or metastatic cancer. One recent example from the laboratory of Driehuys (23) highlights the use of multiple MR technologies including ^{3}He MRI in combination with superparamagnetic iron oxide nanoparticles (SPION) to detect metastatic lung lesions below 1 mm in diameter. Hyperpolarized metabolites, including lactate and glucose, have also been recently reported to be effective at imaging lung pathologies arising from ionizing radiation or lung tumors (127); these methods should open up many new avenues of investigation in lung disease using MRI (145). Taken together, MRI is a powerful and versatile imaging modality to study pulmonary disease at both the bench and bedside.

Although the focus of our review is on preclinical imaging, it is important to mention that MRI technology has recently been used to revise the prevailing paradigm that alveolarization is restricted to fetal life and early childhood. Using ^{3}He MRI, Narayanan et al. (106) have recently shown that the lung grows largely by neoalveolarization through adolescence. The important implication is that the lung may be able to fully recover following injury in early life.

Nuclear Imaging of the Lung: PET and SPECT

Nuclear imaging involves external detectors that can record radiation emitted by radiopharmaceuticals (also called radionuclides or tracers) administered via inhalation, oral ingestion, or intravenous injection. In nuclear medicine, fluorine-18, gallium-67, technetium-99m, thallium-201, and radioactive iodine are commonly used for whole body scanning of the lung, tumors, bone, heart, and thyroid. Because of significant advances made in small animal imaging equipment (130), nuclear methods are no longer restricted to a few major medical centers. In fact, diagnostic and therapeutic nuclear imaging is becoming increasingly utilized and explored in small animal models of lung injury and pulmonary disorders. Nuclear scans can reveal physiological function of the system being investigated; combined with biochemistry, molecular biology, and complementary imaging modalities, nuclear imaging is a powerful tool in investigating cellular, molecular, and systems biology.

Positron emission tomography (PET) and single photon emission computed tomography (SPECT) imaging are widely employed in both clinical and preclinical settings. These modalities allow for both functional and molecular imaging studies, enabling researchers to noninvasively study physiological processes and molecular pathways as they occur in native environments. Modern imaging platforms couple a PET or SPECT detector with an X-ray CT to provide anatomical information and to improve localization of the radiotracers. However, unlike CT, which uses X-rays to construct images, both PET and SPECT modalities require the injection of exogenous contrast agents and are therefore presented together in this section. Small molecules, peptides, proteins, or nanoparticles may be labeled with one or more radioactive atom(s) (32), which upon decay emit high-energy photons that may be detected by PET or SPECT systems.

After injection into a subject under study, these radiolabeled probes will bind or selectively perfuse a target site. Uptake is maximized after receptor binding and/or internalization, or when tracers are actively trapped in the target cell (i.e., tumor cells, inflammatory cells). Unbound probes will be cleared away from nontargeted sites to create image contrast. Since contrast is developed as the tracers wash away from the nontarget tissue, the kinetics of the binding and clearance need to be well matched to the radiotracer employed. For example, antibodies are known to circulate in the blood stream for more than a day, so long-lived isotopes such as ^{89}Zr (PET) or ^{111}In (SPECT) are the optimal reporters for imaging such probes. For rapidly cleared small molecules, such as ammonia, the short half-life of ^{13}N is sufficient to image the uptake, exchange, and clearance from the blood stream. ^{13}N is also commonly used to measure gas exchange (108, 152, 154). The most common radioactive PET and SPECT isotopes, along with half-lives and conjugation methods, are indicated in Table 2.

Like other imaging modalities, SPECT studies should be conducted with consistent injection methods and probe biodistribution/incubation times to maximize the uniformity of uptake and washout properties between animals. In addition, comparing the same organ to a control animal or to the same site on the contralateral side will normalize the data to minimize the effects of minor variations in perfusion. If there is reason to suspect that the disease in question radically changes the perfusion at the target site, a subsequent Tl-201 scan normalizes perfusion differences. In PET imaging, the scan can be acquired in kinetic mode (ideally with the animal subject immobilized), and the entire uptake and washout profile for each site may be simultaneously acquired. The kinetics of

Table 2. *Radiolabeled probes commonly used in PET/SPECT imaging with half-life and conjugation reported*

Isotopes	Half Life	Conjugation
PET		
^{18}F	1.83 h	Covalent
^{11}C	0.34 h	Covalent
^{68}Ga	1.13 h	Chelation
^{15}O	0.03 h	Covalent
^{13}N	0.17 h	Covalent
^{94m}Tc	0.88 h	Chelation
^{89}Zr	3.3 days	Chelation
^{124}I	4.2 days	Covalent
SPECT	Half Life	Conjugation
^{99m}Tc	6.0 h	Chelation
^{111}In	67 h	Chelation
^{123}I, ^{125}I, ^{131}I	13 h, 59 days, 8 days	Covalent
^{67}Ga	78 h	Chelation
^{201}Tl	73 h	Chelation
^{133}Xe	5 days	Unconjugated

PET, positron emission tomography; SPECT, single photon emission computed tomography.

uptake for each site or voxel can then be modeled with use of commercially available software, so that the contribution of perfusion can be normalized between experiments and different sites on the same animal.

The most fundamental differences between PET and SPECT isotopes used in imaging are their decay and emission properties. Upon the decay of the radioactive atoms of a PET probe, a fraction of those events will emit positrons (this fraction is isotope specific), the antimatter of electrons. The positron will travel ~1 mm before it eventually collides with an electron in surrounding tissue (annihilation) to then produce two 511-keV gamma rays given off at ~180 degrees. The mean free path is, however, isotope dependent. To localize the site of radioactive decay, rings of gamma detectors are built and the animal is positioned in the center. PET nuclides are detected via coincident events (161) that occur when two gamma events are recorded within several nanoseconds (generally less than 5). The reconstruction algorithms then use each coincident event to generate a line of response between detectors, with the assumption that the source of each event occurs along each line of response. As more lines of response are built, their points of intersection indicate the source of the activity, and by inference the probe. As a single modality, PET can sufficiently image small rodents; however, coupling PET with CT can be useful to help correct for the attenuation and scatter of events and enhance the accuracy of PET images (42). PET data are quantified through volume of interest analysis (VOI) yielding either an activity per unit volume, expressed as either kBq/cc or standard uptake values (SUV). The SUV expression normalizes uptake for body weight of the animal. Kinetic models of the uptake and washout within a VOI can be calculated if multiple PET scans are performed immediately after probe injection without moving the animal.

SPECT systems localize gamma sources in a manner that is distinct from PET systems. Since SPECT isotopes emit single photons from each decay event, a gamma camera is used to capture a planar image of the radioactive emission from the whole specimen. SPECT detectors are often rotated around the subject to acquire several images at different angles (projections) to create a 3D image, much like in CT. A key component to SPECT is the collimator, which is a filter placed over the gamma camera to dramatically reduce the detection of scattered, nonperpendicular photons. Collimators come in a variety of types including single pinhole, multipinhole, multiplex multipinhole, spiral pinhole, parallel hole, divergent, and convergent. Generally, pinhole collimators are used for higher resolution imaging and multiple-pinhole or parallel collimators are utilized for higher sensitivity but lower resolution imaging. The use of collimators enables SPECT to produce a slightly higher resolution image than PET (~2× better), but at the price of sensitivity (~10× reduction). Data from SPECT image files are usually represented in counts per second per cubic centimeter of volume (cps/cc). These data can also be corrected for attenuation via CT, although the process is more complicated as the corrections need to be calculated for the energy of each SPECT isotope (93). This complication differs from PET attenuation correction, in which each isotope produces pairs of 511-keV gamma, thus requiring only one set of corrections. Kinetic SPECT studies are possible, but either fixed detectors must be used or the process under study must be significantly slower than the acquisition time to acquire a full set of projections.

Nuclear imaging systems can be broadly categorized as stand-alone, bimodal, or trimodal. In a stand-alone imaging system, only the PET or SPECT image is acquired. It is now very common to acquire images by multiple modalities; for example, functional PET and SPECT data are commonly collected with CT scans for anatomical coregistration, albeit physical transport of the animal between systems and subsequent manual processing of experimental outcome are required. Despite these minor drawbacks, most contemporary preclinical imaging instruments are predominately bimodal and are developed with the need for accurate, automatic coregistration between functional, molecular, and anatomical 3D images in mind. These systems typically combine either PET or SPECT with CT or MRI to capitalize on the use of novel emission and transmission properties that each modality has to offer in basic medical science applications and in preclinical research (58, 68, 90, 96). More sophisticated trimodal imaging systems combine PET, SPECT, and CT onto a single platform, as well as the ability to detect dual tracers in the same animal study (28). The combination of nuclear and optical imaging options is also being explored (34–36). However, significant challenges in accurately and rapidly acquiring and reconstructing 3D optical images need to be addressed before the full utility of such a combination can be realized.

In the course of developing novel gene therapy methods for treating lung disorders, such as cystic fibrosis (120, 128), it is necessary to validate the efficacy, location, and duration of transgene expression. Nuclear imaging of transgene expression offers the benefit of noninvasive determination and quantification of the location and magnitude of gene expression, which can also be tracked longitudinally. Of note, the herpes simplex virus type-1 thymidine kinase (HSV1-tk), human somatostatin receptor subtype 2 (SSTR2), and human sodium iodide symporter (hNIS) have been expressed to show the feasibility of nuclear imaging of transgene expression. HSV1-tk and mutants that confer additional selectivity are of particular importance in gene therapy, oncology, and imaging because they convert relatively nontoxic compounds such as penciclovir into their toxic monophosphate esters and phosphorylate radiolabeled thymidine analogs, trapping the analogs in cells enabling an image to be generated (2, 4, 5, 98). This is possible because, unlike the human thymidine kinase, the viral form (HSV1-tk) can efficiently phosphorylate nucleosides and various radioactive derivatives, such as 9-(4-[^{18}F]-fluoro-3-hydroxymethylbutyl) guanine (^{18}F-FHBG) (5). HSV1-tk processing of ^{18}F-FHBG traps this radioisotope inside cells. Accumulation of ^{18}F-FHBG is then detected and quantified by PET imaging, which aids in the positive identification of cells expressing HSV1-tk. Indeed, this has been demonstrated for evaluating the delivery of gene therapy vectors to the lung (125, 159, 160). In a similar manner, stable integration of SSTR2 can be verified by nuclear imaging of internalized ^{111}In-diethylenetriaminepentaacetic acid-Tyr3-octreotate (^{111}In-DTPA-Y3-octreotate) (74). Additionally, ^{94m}Tc-labeled peptides have also been used to image adenoviral delivery to the lungs via PET. Finally, nasal delivery and stable integration of adenoviral vectors expressing hNIS into the lungs of Cottan rats has been imaged by using PET and ^{124}I tracer. In this study, stable integration of hNIS vector was verified up to 17 days postinfection (107).

Together, these studies formulate the foundation for the use of PET and SPECT imaging in monitoring transgene expression, which will invariably advance the prospect of effective gene therapy for pulmonary disorders such as cystic fibrosis.

The most common method for imaging tumors in lung tissue relies on the increased uptake and retention of fluorine-18 fluorodeoxyglucose (^{18}F-FDG). The underlying principle, which allows ^{18}F-FDG to be effectively utilized in nuclear imaging studies, is that rapidly dividing cancerous cells often have a high metabolic rate, requiring elevated glucose uptake and phosphorylation. Since ^{18}F-FDG and glucose are both nonselectively taken up by the same family of glucose transporters, accumulation of ^{18}F-FDG (which cannot be dephosphorylated by cells) allows for nuclear imaging of tumors in the lung (8). Given the complex changes in cellular function in cancerous cells, it is not surprising that inflammation in the lung (discussed below) is a confounding variable that often skews the interpretation and reliability of ^{18}F-FDG incorporation as a sole determinant of lung tumor metastasis. Because of the complications introduced by inflammatory cells (which can also take up ^{18}F-FDG), an alternative compound *O*-(2-[^{18}F]fluoroethyl)-L-tyrosine (^{18}F-FET) has been explored for nuclear imaging of tumors in mice. Although ^{18}F-FET has demonstrated better preferential uptake in tumors vs. inflammatory cells (27), investigators continue to explore alternative markers for specific evaluation of different types of tumors in the lungs. This includes SPECT imaging of small nodule malignancies using ^{111}In-1,4,7,10-tetraazacyclododecane-*N*,*N*′,*N*″,*N*‴-tetraacetic acid-cyclo-(Arg-Gly-Asp-D-Phe-Lys), ^{111}In-DOTA-c(RGDfK) (70). Novel DOTA-neurotensin analogs for PET imaging of non-small cell lung cancer have also been explored following the characterization of high neurotensin binding affinity to its receptor (NTSR1) during the progression of several cancers (7).

Studying ALI in animal models typically involves examining some combination of tissue injury, alteration of the alveolar capillary barrier, inflammatory responses, and quantifiable change in physiological function (99). Nuclear imaging has indeed facilitated several aspects of these studies that examine these main features of lung injury. Similar to oncogenic cells, inflammatory cells also have a high demand for glucose to perform key functions, such as chemotaxis, phagocytosis, and microbial defense (124, 132, 156). As such, ^{18}F-FDG can also be utilized to characterize inflammation, as well as tumorigenic cells (see paragraph above). Importantly, ^{18}F-FDG uptake is primarily confined to neutrophils (as compared with lymphocyte incorporation) in canine and rodent models of lung inflammation (31, 133, 134), and several studies have indeed utilized ^{18}F-FDG to assess the metabolic activity of neutrophils in models of pneumonia and bronchiectasis (30, 80, 81). Radioligands for translocator protein (TSPO; 18 kDa) have also been utilized to detect inflammation in rat models of ALI. TSPO, formerly known as the peripheral-type benzodiazepine receptor, is highly expressed in airway epithelia, submucosal glands, pneumocytes, and alveolar macrophages in the lung. Since TSPO expression in the lung is upregulated during ALI, *N*-benzyl-*N*-methyl-2-[7,8-dihydro-7-(2-[^{18}F]fluoroethyl)-8-oxo-2-phenyl-9H-purin-9-yl]acetamide (^{18}F-FEDAC) and ^{11}C-(R)-[1–2(-chlorophenyl)-*N*-methyl-*N*-(1-methyl-propyl)-3-isoquinolinecarboxyamide] (^{11}C-PK11195) binding to TSPO may be useful for evaluating inflammation in human lungs (67, 69).

The site and extent of bacterial infections can also be tracked in the lungs by use of radioligands. For example, siderophores (500–1,500 Da) are iron-chelating molecules produced by nearly all bacteria, fungi, and some plants. The high binding specificity of some siderophores to ^{68}Ga 3+ (such as ^{68}Ga-triacetylfusarinine C and ^{68}Ga-ferrioxamine) makes siderophore synthesis facile and rapid, and instrumental in imaging bacterial infections in the lung (113, 114).

Nuclear imaging can also be used to monitor lung dysfunction. ^{99m}Tc albumin aggregated (^{99m}Tc-MAA) is prepared from albumin comprised of various particle sizes and is used as a diagnostic SPECT radioisotope. Immediately upon intravenous injection, more than 90% of the ^{99m}Tc-MAA is trapped in the arterioles and capillaries of the lung; as such, distribution of aggregated albumin can be imaged and analyzed as an indicator of regional pulmonary blood flow, emboli, thrombosis, or shunts. Jobse et al. (77) have recently utilized ^{99m}Tc-MAA (injected via the tail vein) in longitudinal in vivo ventilation/perfusion (V/Q) studies to investigate the early effects of mainstream cigarette smoke on BALB/c lung function. V/Q mismatching was detectible as early as 8 wk following 50 min twice daily, 5 days/wk exposure to cigarette smoke. Using this approach, the investigators could detect early pathological changes that lead to chronic obstructive pulmonary disease, which was not as readily detected by standard CT imaging. Nuclear imaging using aerosolized ^{99m}Tc-bound deithylene triamine pentacetate (^{99m}Tc-DTPA) has also proven useful for early detection of pulmonary edema and damage to the alveolar-capillary membrane in burn patients (140, 141). SPECT imaging and ^{99m}Tc-DTPA have also been used to assess airway barrier function in BALB/c mice exposed to house dust mite and methacholine (148). Mucociliary clearance can also be studied by ^{99m}Tc-sulfur colloid and nuclear imaging (20, 56). Earlier detection of V/Q insufficiency, edema, permeability, and mucociliary clearance by nuclear imaging is of course beneficial so that intensive therapy can be instituted at the onset of pulmonary dysfunction.

Preclinical Imaging, Translational Science, and Drug Discovery

The advances made in preclinical imaging have important implications for modern medical practice (15, 16). In a preclinical setting, the imaging modalities discussed herein allow clinicians and researchers the means to fine tune techniques and develop solutions to related problems such as scatter, signal attenuation, and effective probe delivery, prior to patient contact. These problems are especially important to first consider, and then optimize, when examining tissues with differential density and kinetic activity, such as the lung.

Preclinical imaging also facilitates the development of probes with higher degrees of specificity, safety, and diagnostic value. This is an area that has undergone significant development in recent years and holds great promise for the future (15, 16, 55). Of the probes and tracers discussed herein, nuclear imaging probes are most readily transferrable to the clinical setting (as opposed to optical imaging agents). Because of the importance of nuclear imaging in advancing human health and outcomes, there is already a strong infrastructure for radioisotope delivery, synthesis, and imaging across major medical centers located globally. In terms of improving health care

practice, the noninvasive nature of nuclear imaging can provide pulmonologists a more rapid, noninvasive alternative to conventional collection and analysis of bronchoalveolar lavage fluid. Needless to say, noninvasive preclinical imaging can significantly facilitate the studies of pharmacokinetics and pharmacodynamics in the process of drug development and discovery. However, since many contrast agents are administered intravenously, newly developed diagnostic (and possibly even therapeutic) probes must endure regulatory scrutiny, which can further delay the preclinical to clinical translational delivery time.

Conclusion

Noninvasive real-time imaging provides invaluable anatomical, molecular, and functional information in small animal model studies. Arguably, the benefits of being able to repetitively image the lungs, in a longitudinal manner (by either optical, X-ray, MRI, or nuclear modalities) in freely breathing animals outweigh any challenges associated with imaging an air-filled organ undergoing respiratory motion. Continued advancement in the development of bioluminescent reporter systems, fluorescent dyes, radioactive probes, and in vivo animal imaging systems will invariably increase the utility of in vivo imaging in preclinical studies and bridge molecular/biochemical studies with translational research with important clinical applications.

ACKNOWLEDGMENTS

The authors acknowledge helpful assistance provided by Matt Goodson and Dr. Jason Hansen in the preparation of this manuscript. The PAO1-P1-*lux* cells were provided by Dr. Joanna B. Goldberg.

GRANTS

This work was supported in part by a grant awarded by Children's Healthcare of Atlanta to M. N. Helms.

DISCLOSURES

W. M. Leevy currently serves as a consultant for Bruker Biospin. The remaining authors do not have disclosures.

AUTHOR CONTRIBUTIONS

S.T.G., W.M.L., and M.N.H. interpreted results of experiments; S.T.G., N.F., E.M.B., E.O., W.M.L., and M.N.H. prepared figures; S.T.G., N.F., E.M.B., E.O., C.A.D., M.D.B., W.M.L., and M.N.H. drafted manuscript; S.T.G., E.M.B., C.A.D., M.D.B., W.M.L., and M.N.H. edited and revised manuscript; S.T.G., N.F., E.M.B., E.O., C.A.D., M.D.B., W.M.L., and M.N.H. approved final version of manuscript; W.M.L. and M.N.H. conception and design of research; W.M.L. and M.N.H. performed experiments; W.M.L. and M.N.H. analyzed data.

REFERENCES

1. **Abascal JF, Aguirre J, Chamorro-Servent J, Schweiger M, Arridge S, Ripoll J, Vaquero JJ, Desco M.** Influence of absorption and scattering on the quantification of fluorescence diffuse optical tomography using normalized data. *J Biomed Opt* 17: 036013, 2012.
2. **Aghi M, Hochberg F, Breakefield XO.** Prodrug activation enzymes in cancer gene therapy. *J Gene Med* 2: 148–164, 2000.
3. **Akhavan Sharif MR, Lam WW, Ouriadov AV, Holdsworth DW, Santyr GE.** Comparison of hyperpolarized ^{3}He MRI rat lung volume measurement with micro-computed tomography. *NMR Biomed* 23: 359–367, 2010.
4. **Alauddin MM, Gelovani JG.** Pyrimidine nucleosides in molecular PET imaging of tumor proliferation. *Curr Med Chem* 17: 1010–1029, 2010.
5. **Alauddin MM, Shahinian A, Gordon EM, Bading JR, Conti PS.** Preclinical evaluation of the penciclovir analog 9-(4-[^{18}F]fluoro-3-hydroxymethylbutyl)guanine for in vivo measurement of suicide gene expression with PET. *J Nucl Med* 42: 1682–1690, 2001.
6. **Albert MS, Cates GD, Driehuys B, Happer W, Saam B, Springer CS Jr, Wishnia A.** Biological magnetic resonance imaging using laser-polarized 129Xe. *Nature* 370: 199–201, 1994.
7. **Alshoukr F, Prignon A, Brans L, Jallane A, Mendes S, Talbot JN, Tourwe D, Barbet J, Gruaz-Guyon A.** Novel DOTA-neurotensin analogues for 111In scintigraphy and 68Ga PET imaging of neurotensin receptor-positive tumors. *Bioconjug Chem* 22: 1374–1385, 2011.
8. **Ambrosini V, Nanni C, Pettinato C, Fini M, D'Errico A, Trepidi S, Spinelli A, Al-Nahhas A, Rubello D, Zompatori M, Fabbri M, Franchi R, Fanti S.** Assessment of a chemically induced model of lung squamous cell carcinoma in mice by 18F-FDG small-animal PET. *Nucl Med Commun* 28: 647–652, 2007.
9. **Ando Y, Niwa K, Yamada N, Enomoto T, Irie T, Kubota H, Ohmiya Y, Akiyama H.** Firefly bioluminescence quantum yield and colour change by pH-sensitive green emission. *Nature Photonics* 2: 44–47, 2008.
10. **Armitage SE, Pollmann SI, Detombe SA, Drangova M.** Least-error projection sorting to optimize retrospectively gated cardiac micro-CT of free-breathing mice. *Med Phys* 39: 1452–1461, 2012.
11. **Artaechevarria X, Blanco D, de Biurrun G, Ceresa M, Perez-Martin D, Bastarrika G, de Torres JP, Zulueta JJ, Montuenga LM, Ortiz-de-Solorzano C, Munoz-Barrutia A.** Evaluation of micro-CT for emphysema assessment in mice: comparison with non-radiological techniques. *Eur Radiol* 21: 954–962, 2011.
12. **Artaechevarria X, Blanco D, Perez-Martin D, de Biurrun G, Montuenga LM, de Torres JP, Zulueta JJ, Bastarrika G, Munoz-Barrutia A, Ortiz-de-Solorzano C.** Longitudinal study of a mouse model of chronic pulmonary inflammation using breath hold gated micro-CT. *Eur Radiol* 20: 2600–2608, 2010.
13. **Awadh N, Muller NL, Park CS, Abboud RT, FitzGerald JM.** Airway wall thickness in patients with near fatal asthma and control groups: assessment with high resolution computed tomographic scanning. *Thorax* 53: 248–253, 1998.
14. **Badea CT, Guo X, Clark D, Johnston SM, Marshall CD, Piantadosi CA.** Dual-energy micro-CT of the rodent lung. *Am J Physiol Lung Cell Mol Physiol* 302: L1088–L1097, 2012.
15. **Bakhtiar R.** Biomarkers in drug discovery and development. *J Pharmacol Toxicol Methods* 57: 85–91, 2008.
16. **Beckmann N, Laurent D, Tigani B, Panizzutti R, Rudin M.** Magnetic resonance imaging in drug discovery: lessons from disease areas. *Drug Discov Today* 9: 35–42, 2004.
17. **Beckmann N, Tigani B, Ekatodramis D, Borer R, Mazzoni L, Fozard JR.** Pulmonary edema induced by allergen challenge in the rat: noninvasive assessment by magnetic resonance imaging. *Magn Reson Med* 45: 88–95, 2001.
18. **Bell LC, Johnson KM, Fain SB, Wentland A, Drees R, Johnson RA, Bauman G, Francois CJ, Nagle SK.** Simultaneous MRI of lung structure and perfusion in a single breathhold. *J Magn Reson Imaging* 2013 Dec 20. doi: 10.1002/jmri.24520. [Epub ahead of print]
19. **Belur LR, Podetz-Pedersen K, Frandsen J, McIvor RS.** Lung-directed gene therapy in mice using the nonviral Sleeping Beauty transposon system. *Nat Protoc* 2: 3146–3152, 2007.
20. **Bennett WD.** Effect of beta-adrenergic agonists on mucociliary clearance. *J Allergy Clin Immunol* 110: S291–S297, 2002.
21. **Berezin MY, Achilefu S.** Fluorescence lifetime measurements and biological imaging. *Chem Rev* 110: 2641–2684, 2010.
22. **Bottiroli G, Croce AC.** Autofluorescence spectroscopy of cells and tissues as a tool for biomedical diagnosis. *Photochem Photobiol Sci* 3: 189–210, 2004.
23. **Branca RT, Cleveland ZI, Fubara B, Kumar CS, Maronpot RR, Leuschner C, Warren WS, Driehuys B.** Molecular MRI for sensitive and specific detection of lung metastases. *Proc Natl Acad Sci USA* 107: 3693–3697, 2010.
24. **Branchini BR, Ablamsky DM, Murtiashaw MH, Uzasci L, Fraga H, Southworth TL.** Thermostable red and green light-producing firefly luciferase mutants for bioluminescent reporter applications. *Anal Biochem* 361: 253–262, 2007.
25. **Caravan P, Yang Y, Zachariah R, Schmitt A, Mino-Kenudson M, Chen HH, Sosnovik DE, Dai G, Fuchs BC, Lanuti M.** Molecular magnetic resonance imaging of pulmonary fibrosis in mice. *Am J Respir Cell Mol Biol* 49: 1120–1126, 2013.

26. **Carlon M, Toelen J, Van der Perren A, Vandenberghe LH, Reumers V, Sbragia L, Gijsbers R, Baekelandt V, Himmelreich U, Wilson JM, Deprest J, Debyser Z.** Efficient gene transfer into the mouse lung by fetal intratracheal injection of rAAV2/6.2. *Mol Ther* 18: 2130–2138, 2010.
27. **Chang CH, Wang HE, Wu SY, Fan KH, Tsai TH, Lee TW, Chang SR, Liu RS, Chen CF, Chen CH, Fu YK.** Comparative evaluation of FET and FDG for differentiating lung carcinoma from inflammation in mice. *Anticancer Res* 26: 917–925, 2006.
28. **Chapman SE, Diener JM, Sasser TA, Correcher C, Gonzalez AJ, Avermaete TV, Leevy WM.** Dual tracer imaging of SPECT and PET probes in living mice using a sequential protocol. *Am J Nucl Med Mol Imaging* 2: 405–414, 2012.
29. **Chen BT, Brau AC, Johnson GA.** Measurement of regional lung function in rats using hyperpolarized ^{3}helium dynamic MRI. *Magn Reson Med* 49: 78–88, 2003.
30. **Chen DL, Bedient TJ, Kozlowski J, Rosenbluth DB, Isakow W, Ferkol TW, Thomas B, Mintun MA, Schuster DP, Walter MJ.** [^{18}F]fluorodeoxyglucose positron emission tomography for lung antiinflammatory response evaluation. *Am J Respir Crit Care Med* 180: 533–539, 2009.
31. **Chen DL, Schuster DP.** Positron emission tomography with [^{18}F]fluorodeoxyglucose to evaluate neutrophil kinetics during acute lung injury. *Am J Physiol Lung Cell Mol Physiol* 286: L834–L840, 2004.
32. **Chen K, Conti PS.** Target-specific delivery of peptide-based probes for PET imaging. *Adv Drug Deliv Rev* 62: 1005–1022, 2010.
33. **Chen XJ, Hedlund LW, Moller HE, Chawla MS, Maronpot RR, Johnson GA.** Detection of emphysema in rat lungs by using magnetic resonance measurements of ^{3}He diffusion. *Proc Natl Acad Sci USA* 97: 11478–11481, 2000.
34. **Cherry SR.** In vivo molecular and genomic imaging: new challenges for imaging physics. *Phys Med Biol* 49: R13–R48, 2004.
35. **Cherry SR.** Multimodality in vivo imaging systems: twice the power or double the trouble? *Annu Rev Biomed Eng* 8: 35–62, 2006.
36. **Cherry SR.** Multimodality imaging: beyond PET/CT and SPECT/CT. *Semin Nucl Med* 39: 348–353, 2009.
37. **Church JE, Fulton D.** Differences in eNOS activity because of subcellular localization are dictated by phosphorylation state rather than the local calcium environment. *J Biol Chem* 281: 1477–1488, 2006.
38. **Contag CH, Bachmann MH.** Advances in in vivo bioluminescence imaging of gene expression. *Annu Rev Biomed Eng* 4: 235–260, 2002.
39. **Contag CH, Spilman SD, Contag PR, Oshiro M, Eames B, Dennery P, Stevenson DK, Benaron DA.** Visualizing gene expression in living mammals using a bioluminescent reporter. *Photochem Photobiol* 66: 523–531, 1997.
40. **Conti E, Franks NP, Brick P.** Crystal structure of firefly luciferase throws light on a superfamily of adenylate-forming enzymes. *Structure* 4: 287–298, 1996.
41. **Counter WB, Wang IQ, Farncombe TH, Labiris NR.** Airway and pulmonary vascular measurements using contrast-enhanced micro-CT in rodents. *Am J Physiol Lung Cell Mol Physiol* 304: L831–L843, 2013.
42. **D'Ambrosio D, Zagni F, Spinelli AE, Marengo M.** Attenuation correction for small animal PET images: a comparison of two methods. *Comput Math Methods Med* 2013: 103476, 2013.
43. **Dahan M, Laurence T, Pinaud F, Chemla DS, Alivisatos AP, Sauer M, Weiss S.** Time-gated biological imaging by use of colloidal quantum dots. *Opt Lett* 26: 825–827, 2001.
44. **Damron FH, McKenney ES, Schweizer HP, Goldberg JB.** Construction of a broad-host-range Tn7-based vector for single-copy P(BAD)-controlled gene expression in gram-negative bacteria. *Appl Environ Microbiol* 79: 718–721, 2013.
45. **Davison CA, Durbin SM, Thau MR, Zellmer VR, Chapman SE, Diener J, Wathen C, Leevy WM, Schafer ZT.** Antioxidant enzymes mediate survival of breast cancer cells deprived of extracellular matrix. *Cancer Res* 73: 3704–3715, 2013.
46. **Davison CA, Chapman SE, Sasser TA, Wathen C, Diener J, Schafer ZT, Leevy WM.** Multimodal optical, X-ray CT, and SPECT imaging of a mouse model of breast cancer lung metastasis. *Curr Mol Med* 13: 368–376, 2013.
47. **De Langhe E, Vande Velde G, Hostens J, Himmelreich U, Nemery B, Luyten FP, Vanoirbeek J, Lories RJ.** Quantification of lung fibrosis and emphysema in mice using automated micro-computed tomography. *PLoS One* 7: e43123, 2012.
48. **De Langhe E, Vande Velde G, Hostens J, Himmelreich U, Nemery B, Luyten FP, Vanoirbeek J, Lories RJ.** Quantification of lung fibrosis and emphysema in mice using automated micro-computed tomography. *PLoS One* 7: e43123, 2012.
49. **Dikalov S, Griendling KK, Harrison DG.** Measurement of reactive oxygen species in cardiovascular studies. *Hypertension* 49: 717–727, 2007.
50. **Downs CA, Helms MN.** Regulation of ion transport by oxidants. *Am J Physiol Lung Cell Mol Physiol* 305: L595–L603, 2013.
51. **Downs CA, Kriener LH, Yu L, Eaton DC, Jain L, Helms MN.** β-Adrenergic agonists differentially regulate highly selective and nonselective epithelial sodium channels to promote alveolar fluid clearance in vivo. *Am J Physiol Lung Cell Mol Physiol* 302: L1167–L1178, 2012.
52. **Downs CA, Kumar A, Kreiner LH, Johnson NM, Helms MN.** H_2O_2 regulates lung ENaC via ubiquitin-like protein Nedd8. *J Biol Chem* 288: 8136–8145, 2013.
53. **Egger C, Cannet C, Gerard C, Jarman E, Jarai G, Feige A, Suply T, Micard A, Dunbar A, Tigani B, Beckmann N.** Administration of bleomycin via the oropharyngeal aspiration route leads to sustained lung fibrosis in mice and rats as quantified by UTE-MRI and histology. *PLoS One* 8: e63432, 2013.
54. **Farncombe TH.** Software-based respiratory gating for small animal conebeam CT. *Med Phys* 35: 1785–1792, 2008.
55. **Floyd E, McShane TM.** Development and use of biomarkers in oncology drug development. *Toxicol Pathol* 32, *Suppl* 1: 106–115, 2004.
56. **Foster WM, Wagner EM.** Bronchial edema alters ^{99m}Tc-DTPA clearance from the airway surface in sheep. *J Appl Physiol* 91: 2567–2573, 2001.
57. **Fox MS, Ouriadov A, Santyr GE.** Comparison of hyperpolarized He and Xe MRI for the measurement of absolute ventilated lung volume in rats. *Magn Reson Med* 2013 May 6. doi: 10.1002/mrm.24746. [Epub ahead of print]
58. **Franc BL, Acton PD, Mari C, Hasegawa BH.** Small-animal SPECT and SPECT/CT: important tools for preclinical investigation. *J Nucl Med* 49: 1651–1663, 2008.
59. **Francis KP, Yu J, Bellinger-Kawahara C, Joh D, Hawkinson MJ, Xiao G, Purchio TF, Caparon MG, Lipsitch M, Contag PR.** Visualizing pneumococcal infections in the lungs of live mice using bioluminescent *Streptococcus pneumoniae* transformed with a novel gram-positive lux transposon. *Infect Immun* 69: 3350–3358, 2001.
60. **Gammon ST, Leevy WM, Gross S, Gokel GW, Piwnica-Worms D.** Spectral unmixing of multicolored bioluminescence emitted from heterogeneous biological sources. *Anal Chem* 78: 1520–1527, 2006.
61. **Gao X, Cui Y, Levenson RM, Chung LW, Nie S.** In vivo cancer targeting and imaging with semiconductor quantum dots. *Nat Biotechnol* 22: 969–976, 2004.
62. **Goodson P, Kumar A, Jain L, Kundu K, Murthy N, Koval M, Helms MN.** Nadph oxidase regulates alveolar epithelial sodium channel activity and lung fluid balance in vivo via O_2^- signaling. *Am J Physiol Lung Cell Mol Physiol* 302: L410–L419, 2012.
63. **Gould SJ, Subramani S.** Firefly luciferase as a tool in molecular and cell biology. *Anal Biochem* 175: 5–13, 1988.
64. **Gross S, Abraham U, Prior JL, Herzog ED, Piwnica-Worms D.** Continuous delivery of D-luciferin by implanted micro-osmotic pumps enables true real-time bioluminescence imaging of luciferase activity in vivo. *Mol Imaging* 6: 121–130, 2007.
65. **Gross S, Piwnica-Worms D.** Real-time imaging of ligand-induced IKK activation in intact cells and in living mice. *Nat Methods* 2: 607–614, 2005.
66. **Gu L, Hall DJ, Qin Z, Anglin E, Joo J, Mooney DJ, Howell SB, Sailor MJ.** In vivo time-gated fluorescence imaging with biodegradable luminescent porous silicon nanoparticles. *Nat Commun* 4: 2326, 2013.
67. **Hardwick MJ, Chen MK, Baidoo K, Pomper MG, Guilarte TR.** In vivo imaging of peripheral benzodiazepine receptors in mouse lungs: a biomarker of inflammation. *Mol Imaging* 4: 432–438, 2005.
68. **Hasegawa BH, Iwata K, Wong KH, Wu MC, Da Silva AJ, Tang HR, Barber WC, Hwang AH, Sakdinawat AE.** Dual-modality imaging of function and physiology. *Acad Radiol* 9: 1305–1321, 2002.
69. **Hatori A, Yui J, Yamasaki T, Xie L, Kumata K, Fujinaga M, Yoshida Y, Ogawa M, Nengaki N, Kawamura K, Fukumura T, Zhang MR.** PET imaging of lung inflammation with [^{18}F]FEDAC, a radioligand for translocator protein (18 kDa). *PLoS One* 7: e45065, 2012.
70. **Hayakawa T, Mutoh M, Imai T, Tsuta K, Yanaka A, Fujii H, Yoshimoto M.** SPECT/CT of lung nodules using 111In-DOTA-

c(RGDfK) in a mouse lung carcinogenesis model. *Ann Nucl Med* 27: 640–647, 2013.

71. **Hedlund LW, Johnson GA.** Mechanical ventilation for imaging the small animal lung. *ILAR J* 43: 159–174, 2002.
72. **Helms MN, Torres-Gonzalez E, Goodson P, Rojas M.** Direct tracheal instillation of solutes into mouse lung. *J Vis Exp* 42: 1942, 2010.
73. **Hori Y, Takasuka N, Mutoh M, Kitahashi T, Kojima S, Imaida K, Suzuki M, Kohara K, Yamamoto S, Moriyama N, Sugimura T, Wakabayashi K.** Periodic analysis of urethane-induced pulmonary tumors in living A/J mice by respiration-gated X-ray microcomputed tomography. *Cancer Sci* 99: 1774–1777, 2008.
74. **Iyer M, Berenji M, Templeton NS, Gambhir SS.** Noninvasive imaging of cationic lipid-mediated delivery of optical and PET reporter genes in living mice. *Mol Ther* 6: 555–562, 2002.
75. **Jenkins DE, Oei Y, Hornig YS, Yu SF, Dusich J, Purchio T, Contag PR.** Bioluminescent imaging (BLI) to improve and refine traditional murine models of tumor growth and metastasis. *Clin Exp Metastasis* 20: 733–744, 2003.
76. **Jobse BN, Johnson JR, Farncombe TH, Labiris R, Walker TD, Goncharova S, Jordana M.** Evaluation of allergic lung inflammation by computed tomography in a rat model in vivo. *Eur Respir J* 33: 1437–1447, 2009.
77. **Jobse BN, Rhem RG, Wang IQ, Counter WB, Stampfli MR, Labiris NR.** Detection of lung dysfunction using ventilation and perfusion SPECT in a mouse model of chronic cigarette smoke exposure. *J Nucl Med* 54: 616–623, 2013.
78. **Johnson EM, Price RE, Kurie JM, Rivera BS, Cody DD.** A new method for respiratory gating during microcomputed tomography of lung in mice. *J Am Assoc Lab Anim Sci* 47: 46–56, 2008.
79. **Johnson GA, Cofer GP, Hedlund LW, Maronpot RR, Suddarth SA.** Registered ^{1}H and ^{2}He magnetic resonance microscopy of the lung. *Magn Reson Med* 45: 365–370, 2001.
80. **Jones HA, Cadwallader KA, White JF, Uddin M, Peters AM, Chilvers ER.** Dissociation between respiratory burst activity and deoxyglucose uptake in human neutrophil granulocytes: implications for interpretation of ^{18}F-FDG PET images. *J Nucl Med* 43: 652–657, 2002.
81. **Jones HA, Clark RJ, Rhodes CG, Schofield JB, Krausz T, Haslett C.** In vivo measurement of neutrophil activity in experimental lung inflammation. *Am J Respir Crit Care Med* 149: 1635–1639, 1994.
82. **Kazzaz JA, Strayer MS, Wu J, Malone DJ, Koo HC, Shaffer TH, Davis JM, Strayer DS, Wolfson MR.** Perfluorochemical liquid-adenovirus suspensions enhance gene delivery to the distal lung. *Pulm Med* 2011: 918036, 2011.
83. **Kitchen MJ, Lewis RA, Yagi N, Uesugi K, Paganin D, Hooper SB, Adams G, Jureczek S, Singh J, Christensen CR, Hufton AP, Hall CJ, Cheung KC, Pavlov KM.** Phase contrast X-ray imaging of mice and rabbit lungs: a comparative study. *Br J Radiol* 78: 1018–1027, 2005.
84. **Kitchen MJ, Paganin D, Lewis RA, Yagi N, Uesugi K, Mudie ST.** On the origin of speckle in x-ray phase contrast images of lung tissue. *Phys Med Biol* 49: 4335–4348, 2004.
85. **Kitchen M, Paganin D, Lewis R, Yagi N, Uesugi K.** Analysis of speckle patterns in phase-contrast images of lung tissue. *Nucl Instrum Meth A* 548: 240–246, 2005.
86. **Kobayashi S, Fujinawa R, Ota F, Kobayashi S, Angata T, Ueno M, Maeno T, Kitazume S, Yoshida K, Ishii T, Gao C, Ohtsubo K, Yamaguchi Y, Betsuyaku T, Kida K, Taniguchi N.** A single dose of lipopolysaccharide into mice with emphysema mimics human chronic obstructive pulmonary disease exacerbation as assessed by micro-computed tomography. *Am J Respir Cell Mol Biol* 49: 971–977, 2013.
87. **Kocher B, Piwnica-Worms D.** Illuminating cancer systems with genetically engineered mouse models and coupled luciferase reporters in vivo. *Cancer Discov* 3: 616–629, 2013.
88. **Kundu K, Knight SF, Willett N, Lee S, Taylor WR, Murthy N.** Hydrocyanines: a class of fluorescent sensors that can image reactive oxygen species in cell culture, tissue, and in vivo. *Angew Chem Int Ed Engl* 48: 299–303, 2009.
89. **Lam WW, Holdsworth DW, Du LY, Drangova M, McCormack DG, Santyr GE.** Micro-CT imaging of rat lung ventilation using continuous image acquisition during xenon gas contrast enhancement. *J Appl Physiol* 103: 1848–1856, 2007.
90. **Lang TF, Hasegawa BH, Liew SC, Brown JK, Blankespoor SC, Reilly SM, Gingold EL, Cann CE.** Description of a prototype emission-transmission computed tomography imaging system. *J Nucl Med* 33: 1881–1887, 1992.
91. **Lederlin M, Ozier A, Dournes G, Ousova O, Girodet PO, Begueret H, Marthan R, Montaudon M, Laurent F, Berger P.** In vivo micro-CT assessment of airway remodeling in a flexible OVA-sensitized murine model of asthma. *PLoS One* 7: e48493, 2012.
92. **Lederlin M, Ozier A, Montaudon M, Begueret H, Ousova O, Marthan R, Berger P, Laurent F.** Airway remodeling in a mouse asthma model assessed by in-vivo respiratory-gated micro-computed tomography. *Eur Radiol* 20: 128–137, 2010.
93. **Lee HH, Chen JC.** Investigation of attenuation correction for small animal single photon emission computed tomography. *Comput Math Methods Med* 430276, 2013.
94. **Lee HW, Jeon YH, Hwang MH, Kim JE, Park TI, Ha JH, Lee SW, Ahn BC, Lee J.** Dual reporter gene imaging for tracking macrophage migration using the human sodium iodide symporter and an enhanced firefly luciferase in a murine inflammation model. *Mol Imaging Biol* 15: 703–712, 2013.
95. **Lewis RA, Yagi N, Kitchen MJ, Morgan MJ, Paganin D, Siu KK, Pavlov K, Williams I, Uesugi K, Wallace MJ, Hall CJ, Whitley J, Hooper SB.** Dynamic imaging of the lungs using x-ray phase contrast. *Phys Med Biol* 50: 5031–5040, 2005.
96. **Liew SC, Hasegawa BH.** Noise, resolution, and sensitivity considerations in the design of a single-slice emission-transmission computed tomographic system. *Med Phys* 18: 1002–1015, 1991.
97. **Luangsay S, Wittamer V, Bondue B, De Henau O, Rouger L, Brait M, Franssen JD, de Nadai P, Huaux F, Parmentier M.** Mouse ChemR23 is expressed in dendritic cell subsets and macrophages, and mediates an anti-inflammatory activity of chemerin in a lung disease model. *J Immunol* 183: 6489–6499, 2009.
98. **Luker GD, Sharma V, Pica CM, Dahlheimer JL, Li W, Ochesky J, Ryan CE, Piwnica-Worms H, Piwnica-Worms D.** Noninvasive imaging of protein-protein interactions in living animals. *Proc Natl Acad Sci USA* 99: 6961–6966, 2002.
99. **Matute-Bello G, Downey G, Moore BB, Groshong SD, Matthay MA, Slutsky AS, Kuebler WM.** An official American Thoracic Society workshop report: features and measurements of experimental acute lung injury in animals. *Am J Respir Cell Mol Biol* 44: 725–738, 2011.
100. **Mclean AN, Sproule MW, Cowan MD, Thomson NC.** High resolution computed tomography in asthma. *Thorax* 53: 308–314, 1998.
101. **Meighen EA.** Molecular biology of bacterial bioluminescence. *Microbiol Rev* 55: 123–142, 1991.
102. **Mistry NN, Pollaro J, Song J, De LM, Johnson GA.** Pulmonary perfusion imaging in the rodent lung using dynamic contrast-enhanced MRI. *Magn Reson Med* 59: 289–297, 2008.
103. **Mizgerd JP, Skerrett SJ.** Animal models of human pneumonia. *Am J Physiol Lung Cell Mol Physiol* 294: L387–L398, 2008.
104. **Mora AL, LaVoy J, McKean M, Stecenko A, Brigham KL, Parker R, Rojas M.** Prevention of NF-κB activation in vivo by a cell-permeable NF-κB inhibitor peptide. *Am J Physiol Lung Cell Mol Physiol* 289: L536–L544, 2005.
105. **Namati E, Thiesse J, Sieren JC, Ross A, Hoffman EA, McLennan G.** Longitudinal assessment of lung cancer progression in the mouse using in vivo micro-CT imaging. *Med Phys* 37: 4793–4805, 2010.
106. **Narayanan M, Owers-Bradley J, Beardsmore CS, Mada M, Ball I, Garipov R, Panesar KS, Kuehni CE, Spycher BD, Williams SE, Silverman M.** Alveolarization continues during childhood and adolescence: new evidence from helium-3 magnetic resonance. *Am J Respir Crit Care Med* 185: 186–191, 2012.
107. **Niu G, Krager KJ, Graham MM, Hichwa RD, Domann FE.** Noninvasive radiological imaging of pulmonary gene transfer and expression using the human sodium iodide symporter. *Eur J Nucl Med Mol Imaging* 32: 534–540, 2005.
108. **O'Neill K, Venegas JG, Richter T, Harris RS, Layfield JD, Musch G, Winkler T, Melo MF.** Modeling kinetics of infused ^{13}NN-saline in acute lung injury. *J Appl Physiol* 95: 2471–2484, 2003.
109. **Orndorff RL, Hong N, Yu K, Feinstein SI, Zern BJ, Fisher AB, Muzykantov VR, Chatterjee S.** NOX2 in lung inflammation: quantum dot based in situ imaging of NOX2-mediated expression of vascular cell adhesion molecule-1. *Am J Physiol Lung Cell Mol Physiol* 306: L260–L268, 2014.
110. **Overhage J, Lewenza S, Marr AK, Hancock RE.** Identification of genes involved in swarming motility using a Pseudomonas aeruginosa PAO1 mini-Tn5-lux mutant library. *J Bacteriol* 189: 2164–2169, 2007.

111. **Paulus MJ, Gleason SS, Kennel SJ, Hunsicker PR, Johnson DK.** High resolution X-ray computed tomography: an emerging tool for small animal cancer research. *Neoplasia* 2: 62–70, 2000.
112. **Peces-Barba G, Ruiz-Cabello J, Cremillieux Y, Rodriguez I, Dupuich D, Callot V, Ortega M, Rubio Arbo ML, Cortijo M, Gonzalez-Mangado N.** Helium-3 MRI diffusion coefficient: correlation to morphometry in a model of mild emphysema. *Eur Respir J* 22: 14–19, 2003.
113. **Petrik M, Haas H, Dobrozemsky G, Lass-Florl C, Helbok A, Blatzer M, Dietrich H, Decristoforo C.** ^{68}Ga-siderophores for PET imaging of invasive pulmonary aspergillosis: proof of principle. *J Nucl Med* 51: 639–645, 2010.
114. **Petrik M, Haas H, Schrettl M, Helbok A, Blatzer M, Decristoforo C.** In vitro and in vivo evaluation of selected ^{68}Ga-siderophores for infection imaging. *Nucl Med Biol* 39: 361–369, 2012.
115. **Postnov AA, Meurrens K, Weiler H, Van Dyck D, Xu H, Terpstra P, De Clerck NM.** In vivo assessment of emphysema in mice by high resolution X-ray microtomography. *J Microsc* 220: 70–75, 2005.
116. **Prasad MN, Brown MS, Ahmad S, Abtin F, Allen J, da Costa I, Kim HJ, McNitt-Gray MF, Goldin JG.** Automatic segmentation of lung parenchyma in the presence of diseases based on curvature of ribs. *Acad Radiol* 15: 1173–1180, 2008.
117. **Prescher JA, Contag CH.** Guided by the light: visualizing biomolecular processes in living animals with bioluminescence. *Curr Opin Chem Biol* 14: 80–89, 2010.
118. **Pu J, Roos J, Yi CA, Napel S, Rubin GD, Paik DS.** Adaptive border marching algorithm: automatic lung segmentation on chest CT images. *Comput Med Imaging Graph* 32: 452–462, 2008.
119. **Qian F, Deng J, Gantner BN, Flavell RA, Dong C, Christman JW, Ye RD.** Map kinase phosphatase 5 protects against sepsis-induced acute lung injury. *Am J Physiol Lung Cell Mol Physiol* 302: L866–L874, 2012.
120. **Rab A, Rowe SM, Raju SV, Bebok Z, Matalon S, Collawn JF.** Cigarette smoke and CFTR: implications in the pathogenesis of COPD. *Am J Physiol Lung Cell Mol Physiol* 305: L530–L541, 2013.
121. **Radotic K, Radenovic C, Jeremic M.** Spontaneous ultraweak bioluminescence in plants: origin, mechanisms and properties. *Gen Physiol Biophys* 17: 289–308, 1998.
122. **Ramirez MP, Sigaloff KC, Kubatina LV, Donahue MA, Venkatesh AK, Albert MS.** Physiological response of rats to delivery of helium and xenon: implications for hyperpolarized noble gas imaging. *NMR Biomed* 13: 253–264, 2000.
123. **Rao J, Dragulescu-Andrasi A, Yao H.** Fluorescence imaging in vivo: recent advances. *Curr Opin Biotechnol* 18: 17–25, 2007.
124. **Reidy MF, Wright JR.** Surfactant protein A enhances apoptotic cell uptake and TGF-beta1 release by inflammatory alveolar macrophages. *Am J Physiol Lung Cell Mol Physiol* 285: L854–L861, 2003.
125. **Richard JC, Zhou Z, Ponde DE, Dence CS, Factor P, Reynolds PN, Luker GD, Sharma V, Ferkol T, Piwnica-Worms D, Schuster DP.** Imaging pulmonary gene expression with positron emission tomography. *Am J Respir Crit Care Med* 167: 1257–1263, 2003.
126. **Ritman EL.** Current status of developments and applications of micro-CT. *Annu Rev Biomed Eng* 13: 531–552, 2011.
127. **Rodrigues TB, Serrao EM, Kennedy BW, Hu DE, Kettunen MI, Brindle KM.** Magnetic resonance imaging of tumor glycolysis using hyperpolarized C-labeled glucose. *Nat Med* 20: 93–97, 2013.
128. **Rogers CS, Abraham WM, Brogden KA, Engelhardt JF, Fisher JT, McCray PB Jr, McLennan G, Meyerholz DK, Namati E, Ostedgaard LS, Prather RS, Sabater JR, Stoltz DA, Zabner J, Welsh MJ.** The porcine lung as a potential model for cystic fibrosis. *Am J Physiol Lung Cell Mol Physiol* 295: L240–L263, 2008.
129. **Salerno M, Altes TA, Brookeman JR, de Lange EE, Mugler JP III.** Dynamic spiral MRI of pulmonary gas flow using hyperpolarized ^{3}He: preliminary studies in healthy and diseased lungs. *Magn Reson Med* 46: 667–677, 2001.
130. **Sanchez F, Orero A, Soriano A, Correcher C, Conde P, Gonzalez A, Hernandez L, Moliner L, Rodriguez-Alvarez MJ, Vidal LF, Benlloch JM, Chapman SE, Leevy WM.** ALBIRA: a small animal PETSPECTCT imaging system. *Med Phys* 40: 051906, 2013.
131. **Sanz P, Teel LD, Alem F, Carvalho HM, Darnell SC, O'Brien AD.** Detection of *Bacillus anthracis* spore germination in vivo by bioluminescence imaging. *Infect Immun* 76: 1036–1047, 2008.
132. **Schagat TL, Wofford JA, Greene KE, Wright JR.** Surfactant protein A differentially regulates peripheral and inflammatory neutrophil chemotaxis. *Am J Physiol Lung Cell Mol Physiol* 284: L140–L147, 2003.
133. **Schuster DP, Brody SL, Zhou Z, Bernstein M, Arch R, Link D, Mueckler M.** Regulation of lipopolysaccharide-induced increases in neutrophil glucose uptake. *Am J Physiol Lung Cell Mol Physiol* 292: L845–L851, 2007.
134. **Schuster DP, Kozlowski J, Hogue L.** Imaging lung inflammation in a murine model of Pseudomonas infection: a positron emission tomography study. *Exp Lung Res* 29: 45–57, 2003.
135. **Sen SK, Jin X, Holzner C, Narayanan S, Liu B, Wang D, Agah M, Wang L, Yu H, Wang G.** Experimental studies on few-view reconstruction for high-resolution micro-CT. *J Xray Sci Technol* 21: 25–42, 2013.
136. **Shaner NC, Steinbach PA, Tsien RY.** A guide to choosing fluorescent proteins. *Nat Methods* 2: 905–909, 2005.
137. **Signore A, Mather SJ, Piaggio G, Malviya G, Dierckx RA.** Molecular imaging of inflammation/infection: nuclear medicine and optical imaging agents and methods. *Chem Rev* 110: 3112–3145, 2010.
138. **Slavinsky AA.** Index of phagocyte activation based on luminescence of dehydrogenase coenzymes. *Folia Haematol Int Mag Klin Morphol Blutforsch* 117: 365–368, 1990.
139. **Sluimer I, Prokop M, van Ginneken B.** Toward automated segmentation of the pathological lung in CT. *IEEE Trans Med Imaging* 24: 1025–1038, 2005.
140. **Sundram FX.** Clinical studies of alveolar-capillary permeability using technetium-99m DTPA aerosol. *Ann Nucl Med* 9: 171–178, 1995.
141. **Sundram FX, Lee ST.** Radionuclide lung scanning in the management of respiratory burns. *Ann Acad Med Singapore* 21: 630–634, 1992.
142. **Takahashi M, Togao O, Obara M, van Cauteren M, Ohno Y, Doi S, Kuro-o M, Malloy C, Hsia CC, Dimitrov I.** Ultra-short echo time (UTE) MR imaging of the lung: comparison between normal and emphysematous lungs in mutant mice. *J Magn Reson Imaging* 32: 326–333, 2010.
143. **Takemura Y, Helms MN, Eaton AF, Self J, Ramosevac S, Jain L, Bao HF, Eaton DC.** Cholinergic regulation of epithelial sodium channels in rat alveolar type 2 epithelial cells. *Am J Physiol Lung Cell Mol Physiol* 304: L428–L437, 2013.
144. **Taschereau R, Chow PL, Chatziioannou AF.** Monte carlo simulations of dose from microCT imaging procedures in a realistic mouse phantom. *Med Phys* 33: 216–224, 2006.
145. **Thind K, Chen A, Friesen-Waldner L, Ouriadov A, Scholl TJ, Fox M, Wong E, Vandyk J, Hope A, Santyr G.** Detection of radiation-induced lung injury using hyperpolarized ^{13}C magnetic resonance spectroscopy and imaging. *Magn Reson Med* 70: 601–609, 2013.
146. **Thind K, Jensen MD, Hegarty E, Chen AP, Lim H, Martinez-Santiesteban F, Van Dyk J, Wong E, Scholl TJ, Santyr GE.** Mapping metabolic changes associated with early Radiation Induced Lung Injury post conformal radiotherapy using hyperpolarized C-pyruvate Magnetic Resonance Spectroscopic Imaging. *Radiother Oncol* 110: 317–322, 2014.
147. **Tigani B, Schaeublin E, Sugar R, Jackson AD, Fozard JR, Beckmann N.** Pulmonary inflammation monitored noninvasively by MRI in freely breathing rats. *Biochem Biophys Res Commun* 292: 216–221, 2002.
148. **Turi GJ, Ellis R, Wattie JN, Labiris NR, Inman MD.** The effects of inhaled house dust mite on airway barrier function and sensitivity to inhaled methacholine in mice. *Am J Physiol Lung Cell Mol Physiol* 300: L185–L190, 2011.
149. **van Rikxoort EM, de Hoop B, Viergever MA, Prokop M, van Ginneken B.** Automatic lung segmentation from thoracic computed tomography scans using a hybrid approach with error detection. *Med Phys* 36: 2934–2947, 2009.
150. **van Rikxoort EM, van Ginneken B.** Automated segmentation of pulmonary structures in thoracic computed tomography scans: a review. *Phys Med Biol* 58: R187–R220, 2013.
151. **Vasilescu DM, Gao Z, Saha PK, Yin L, Wang G, Haefeli-Bleuer B, Ochs M, Weibel ER, Hoffman EA.** Assessment of morphometry of pulmonary acini in mouse lungs by nondestructive imaging using multiscale microcomputed tomography. *Proc Natl Acad Sci USA* 109: 17105–17110, 2012.
152. **Venegas J, Winkler T, Harris RS.** Lung physiology and aerosol deposition imaged with positron emission tomography. *J Aerosol Med Pulm Drug Deliv* 26: 1–8, 2013.
153. **Virostko J, Chen Z, Fowler M, Poffenberger G, Powers AC, Jansen ED.** Factors influencing quantification of in vivo bioluminescence imaging: application to assessment of pancreatic islet transplants. *Mol Imaging* 3: 333–342, 2004.

154. **Wellman TJ, Winkler T, Costa EL, Musch G, Harris RS, Venegas JG, Melo MF.** Measurement of regional specific lung volume change using respiratory-gated PET of inhaled ^{13}N-nitrogen. *J Nucl Med* 51: 646–653, 2010.
155. **Willekens I, Buls N, Lahoutte T, Baeyens L, Vanhove C, Caveliers V, Deklerck R, Bossuyt A, de Mey J.** Evaluation of the radiation dose in micro-CT with optimization of the scan protocol. *Contrast Media Mol Imaging* 5: 201–207, 2010.
156. **Williams AE, Chambers RC.** The mercurial nature of neutrophils: still an enigma in ARDS? *Am J Physiol Lung Cell Mol Physiol* 306: L217–L230, 2014.
157. **Xiang JJ, Tang JQ, Zhu SG, Nie XM, Lu HB, Shen SR, Li XL, Tang K, Zhou M, Li GY.** IONP-PLL: a novel non-viral vector for efficient gene delivery. *J Gene Med* 5: 803–817, 2003.
158. **Xu T, Ducote JL, Wong JT, Molloi S.** Dynamic dual-energy chest radiography: a potential tool for lung tissue motion monitoring and kinetic study. *Phys Med Biol* 56: 1191–1205, 2011.
159. **Yaghoubi S, Barrio JR, Dahlbom M, Iyer M, Namavari M, Satyamurthy N, Goldman R, Herschman HR, Phelps ME, Gambhir SS.** Human pharmacokinetic and dosimetry studies of [^{18}F]FHBG: a reporter probe for imaging herpes simplex virus type-1 thymidine kinase reporter gene expression. *J Nucl Med* 42: 1225–1234, 2001.
160. **Yaghoubi SS, Gambhir SS.** PET imaging of herpes simplex virus type 1 thymidine kinase (HSV1-tk) or mutant HSV1-sr39tk reporter gene expression in mice and humans using [^{18}F]FHBG. *Nat Protoc* 1: 3069–3075, 2006.
161. **Yao R, Lecomte R, Crawford ES.** Small-animal PET: what is it, and why do we need it? *J Nucl Med Technol* 40: 157–165, 2012.
162. **Ziady AG, Kotlarchyk M, Bryant L, McShane M, Lee Z.** Bioluminescent imaging of reporter gene expression in the lungs of wildtype and model mice following the administration of PEG-stabilized DNA nanoparticles. *Microsc Res Tech* 73: 918–928, 2010.
163. **Zurek M, Cremillieux Y.** MRI of the lung: non-invasive protocols and applications to small animal models of lung disease. *Methods Mol Biol* 771: 459–474, 2011.